# Electrically-Tunable Light-Matter Interactions in Quantum Materials

Thesis by

William Schuyler Whitney

In Partial Fulfillment of the Requirements for
the degree of
Doctor of Philosophy

CALIFORNIA INSTITUTE OF TECHNOLOGY
Pasadena, California

2019
(Defended September 27, 2018)

© 2019

William Schuyler Whitney
ORCID: 0000-0001-5269-2967

# Acknowledgements

To start, I would like to acknowledge everyone who encouraged me to find my way to Caltech. As an undergraduate with no lab experience, Professor Eric Mazur at Harvard was kind enough to let me join his research group for a summer, and learn from his students and postdocs. At Cornell, Professor Paul McEuen was a great inspiration. My graduate student mentors while working in his group, Arend van der Zande and Jonathan Alden, were indispensable role models and sources of knowledge. Professor Keith Schwab, now a member of my thesis committee at Caltech, was a fantastic mentor to me and a number of other students. Before any of that, my great uncle, Professor Charles Whitney, and aunt, Meredith Whitney, provided examples of practicing scientists passionate about their work and worlds.

Second, I would like to acknowledge my thesis advisor, Professor Harry Atwater. Harry is an endlessly impressive scientist, mentor, and person, and it has been a privilege and joy to work with and learn from him these past six years. Beyond the generous encouragement, creative freedom, and scientific mentoring he provides, Harry is a kind and caring advisor, and I thank him for his support.

I further acknowledge the entirety of my thesis and candidacy committees, for their time and mentorship. In particular, Professor Keith Schwab helped convince me to come to Caltech, supported me as a first year student, and is a great friend. Professor George Rossman is a tremendous teacher, and imparted to me nearly everything I know about infrared spectroscopy.

I have great respect and admiration for my colleagues at Caltech and elsewhere, and would not have been able to produce the contents of this thesis without them. Victor Brar, now a professor at the University of Wisconsin, was a superlative mentor and, more importantly, person. Working with him was a great pleasure. Deep Jariwala, now a professor at the University of Pennsylvania, was an invaluable asset to the Atwater group during his time at Caltech, and enabled much of our present work on two-dimensional materials. Michelle

Sherrott was a fantastic coauthor and collaborator in several projects, all of which were improved by her partnership. I owe a great deal of gratitude to a large number of other colleagues and collaborators, a subset of whom I thank here: Zak Al-Balushi, Muhammad Alam, Dimitri Basov, Hans Bechtel, Souvik Biswas, Artur Davoyan, Guy DeRose, Dagny Fleischman, Kate Fountaine, Rebecca Glaudell, Max Jones, Seyoon Kim, Yonghwi Kim, Emily Kosten, Wei-Hsiang Lin, Kelly Mauser, Yunbo Ou, Matt Sheldon, Ruzan Sokhoyan, Matt Sullivan, Yulia Tolstova, Cora Went, Joeson Wong, Pin Chieh Wu, and Arky Yang.

I greatly appreciate the love and support of my parents, Nan and Garret, throughout my time at Caltech, and the efforts they went to to provide me a life that could lead here. I thank my wife, Sarah. She is the heart of my life, and a spring of encouragement. I say with no hyperbole that none of this would have been possible without her. Together, we met many friends here, all of whom have touched and enriched our lives, and made the past six years a time we will hold dear.

# Abstract

Dynamic control of the flow of light at the nanoscale is critical for next-generation optoelectronic devices that will enable the technologies of the future. Ultra-thin, layered materials are promising building blocks for this functionality, as they are easily fabricated into atom-scale structures, and their optical properties change dramatically under applied electric fields. Many of these material systems, like topological insulators – a subset of layered materials that host spin-polarized surface states, promise more exotic functionality as well. The emerging field of nanophotonics in quantum materials is a route not only to an improved material platform for optoelectronics, but also to new physics, and the potential new device paradigms that follow.

In this work we describe investigations of electrically-tunable light-matter interactions in two different layered materials: few-layer black phosphorus, and bismuth antimony telluride. In few-layer black phosphorus, we demonstrate several in-plane anisotropic optoelectronic phenomena, including Pauli-blocking of intersubband optical transitions under carrier injection, a quantum-confined Stark effect, and a change of quantum well selection rules under applied electric field. We further describe how these optoelectronic phenomena drive anisotropic birefringence and dichroism in few-layer black phosphorus. Lastly, we present theory describing amplitude, phase and polarization control in a black phosphorus integrated microcavity device, with applications that include metasurface beam-steering and more.

We next present experiments demonstrating field-effect control of optical transitions in bismuth antimony telluride. These measurements evidence the merits of topological insulators as optoelectronic materials, and highlight a pathway towards future exploration of spin-plasmon excitations in bismuth antimony telluride.

Lastly, we present a summary of pending work, including initial results of an ongoing study of plasmon excitations in few-layer black phosphorus, and a perspective on next steps for both these projects and nanophotonics in quantum materials at large.

# Published Content and Contributions

Portions of this thesis have been drawn from the following publications:

Michelle C. Sherrott*, **William S. Whitney***, Deep Jariwala, Souvik Biswas, Cora M. Went, Joeson Wong, George R. Rossman, and Harry A. Atwater. "Anisotropic Quantum Well Electro-Optics in Few-Layer Black Phosphorus." *Nano Letters* 19 (1), 269-276 (2019). DOI: 10.1021/acs.nanolett.8b03876.
***Equal author contributors**
W.S.W and M.C.S conceived the experiment together, designed and fabricated the devices, performed the measurements, and prepared the manuscript, all together with coauthors.

Harry A. Atwater, Artur R. Davoyan, Ognjen Ilic, Deep Jariwala, Michelle C. Sherrott, Cora M. Went, **William S. Whitney**, and Joeson Wong. "Materials Challenges for the Starshot Lightsail." *Nature Materials* 17, 861-867 (2018). DOI: 10.1038/s41563-018-0075-8.
All authors conceived the project, led by H.A.A. All authors performed calculations and performed the manuscript.

**William S. Whitney***, Michelle C. Sherrott*, Deep Jariwala, Wei-Hsiang Lin, Hans A. Bechtel, George R. Rossman, and Harry A. Atwater. "Field Effect Optoelectronic Modulation of Quantum-Confined Carriers in Black Phosphorus." *Nano Letters* 17 (1), 78–84 (2017). DOI: 10.1021/acs.nanolett.6b03362.
***Equal author contributors**
W.S.W. and M.C.S. conceived the experiment together, designed and fabricated the devices, performed the measurements, and prepared the manuscript, all together with coauthors.

**William S. Whitney**, Victor W. Brar, Yunbo Ou, Yinming Shao, Artur R. Davoyan, Dimitri N. Basov, Ke He, Qi-Kun Xue, and Harry A. Atwater. "Gate-Variable Mid-Infrared Optical Transitions in a $(Bi_{1-x}Sb_x)_2Te_3$ Topological Insulator." *Nano Letters* 17 (1), 255-260 (2017). DOI: 10.1021/acs.nanolett.6b03992.
W.S.W. and V.W.B. conceived the experiment together, together with H.A.A. W.S.W designed and fabricated the devices, performed the measurements, and prepared the manuscript, together with coauthors. Y.O. grew the sample films.

Katherine T. Fountaine, **William S. Whitney** and Harry A. Atwater. "Resonant Absorption in Semiconductor Nanowires and Nanowire Arrays: Relating Leaky Waveguide Modes to Bloch Photonic Crystal Modes." *Journal of Applied Physics* 116 (15), 153106 (2014). DOI: 10.1063/1.4898758.
K.T.F. and H.A.A. conceived the experiment. K.T.F and W.S.W performed the calculations and prepared the manuscript.

# Table of Contents

Acknowledgements ..................................................... iii
Abstract ..................................................... v
Published Content and Contributions ..................................................... vi
Table of Contents ..................................................... vii
List of Figures ..................................................... ix
1 Introduction ..................................................... 1
1.1 The Case for Active Nanophotonics ..................................................... 2
1.2 Van der Waals Materials ..................................................... 4
1.3 Topological Materials ..................................................... 6
1.4 The Scope of this Thesis ..................................................... 8
2 Charge-Driven Modulation of Intersubband Optical Transitions in Few-Layer Black Phosphorus ..................................................... 10
2.1 Introduction ..................................................... 11
2.2 Experimental Measurements of the Black Phosphorus Optical Response with Doping by an Electrostatic Gate ..................................................... 12
2.2.1 7 nm Flake with Light Doping ..................................................... 13
2.2.2 14 nm Flake with Light Doping ..................................................... 17
2.2.3 6.5 nm Flake with Heavy Doping ..................................................... 19
2.3 Conclusion ..................................................... 23
3 Field-Driven Modulation of Absorption and Anisotropy in Few-Layer Black Phosphorus ..................................................... 24
3.1 Introduction ..................................................... 25
3.2 Experimental Measurements of the Black Phosphorus Optical Response with an Applied Electric Field ..................................................... 26
3.2.1 3.5 nm Flake ..................................................... 28
3.2.2 8.5 nm Flake ..................................................... 31

3.2.3 Visible Frequency Modulation ........ 33
3.3 Conclusions ........ 35
4 Gate-Variable Inter and Intraband Optical Transitions in a Bismuth Antimony Telluride Topological Insulator ........ 36
4.1 Introduction ........ 37
4.2 Experimental Measurements of the Bismuth Antimony Telluride Optical Response with Doping by an Electrostatic Gate ........ 38
4.2.1 Epitaxial Lift-Off of Bismuth Antimony Telluride ........ 39
4.2.2 Infrared Optical Response ........ 40
4.2.3 Transport Characterization ........ 42
4.2.4 5 K Measurements ........ 45
4.3 Dielectric Function and Transfer Matrix Model ........ 46
4.4 Conclusions ........ 49
5 Phase, Amplitude and Polarization Modulation in Few-Layer Black Phosphorus Microcavities ........ 50
5.1 Introduction ........ 51
5.2 Theory Results for Phase, Amplitude and Polarization Modulation ........ 53
5.3 Conclusions ........ 57
6 Ongoing and Future Work and Perspective ........ 58
6.1 Ongoing and Future Work ........ 59
6.1.1 Plasmons in Few-Layer Black Phosphorus ........ 59
6.1.2 Phase Modulation and Beam Steering in Black Phosphorus ........ 65
6.1.3 Spin-Plasmons in Bismuth Antimony Telluride ........ 67
6.2 Perspective ........ 69
Bibliography ........ 71
Appendix A: Nanofabrication Methods ........ 76
Appendix B: Calculation Methods ........ 81

# List of Figures

1.1 Schematic examples of static metasurfaces ........ 3
1.2 Overview of optoelectronic properties of van der Waals materials ...... 5
1.3 Crystal and electronic band structure of bismuth antimony telluride ... 7
2.1 Schematic of black phosphorus field-effect infrared transmission modulation experiment and band structure ........ 13
2.2 Lightly doped 7 nm black phosphorus: field-effect infrared and electrical modulation results, proposed theory model, and optical image ........ 15
2.3 Lightly doped 14 nm black phosphorus: field-effect infrared and electrical modulation results, proposed theory model, and optical image ........ 18
2.4 Heavily doped 6.5 nm black phosphorus: field-effect infrared and electrical modulation results, proposed theory model, and optical image ........ 19
3.1 Schematic of field and charge-driven electro-optical effects in few-layer black phosphorus, and schematic of device to separate and probe them ........ 28
3.2 3.5 nm black phosphorus: anisotropic field and charge-driven infrared modulation, complex refractive index model, and optical image ........ 29
3.3 8.5 nm black phosphorus: anisotropic field and charge-driven infrared modulation, complex refractive index model, and optical image ........ 32
3.4 Visible frequency optical modulation in few-layer black phosphorus: device design, anisotropic optical modulation results, complex refractive index model, and optical image ........ 34

4.1 Schematic of concept, device and experimental design for field-effect modulation of optical transitions in bismuth antimony telluride, and atomic force microscopy characterization .................... 39
4.2 Epitaxial lift-off of bismuth antimony telluride: method and results. 40
4.3 Gate-variable infrared reflectance and transmittance results for bismuth antimony telluride, proposed theory, and transfer matrix model theory results ................................................................ 41
4.4 Electrical characterization of gate-driven metallic to insulating behavior transition, and schematic angle-resolved photoemission spectroscopy results ................................................................ 43
4.5 T = 5 K gate-variable infrared transmittance results for bismuth antimony telluride ................................................................ 46
4.6 Schematic of band-bending effects in bismuth antimony telluride field-effect devices ................................................................ 48
5.1 Schematic of 1D, active metasurface for optical beam-steering ........ 52
5.2 Few-layer black phosphorus phase modulator device schematic and calculation results, and complex refractive index model ................... 54
5.3 Reflected phase modulation and reflectance calculation results as a function of microcavity quality factor ................................................ 55
5.4 Few-layer black phosphorus amplitude modulator device schematic and calculation results, and complex refractive index model ............ 56
6.1 Calculated complex dielectric function for 5 nm black phosphorus along armchair and zigzag crystal axes as a function of carrier density, and identification of hyperbolic regime ............................... 61
6.2 Schematic of gate-tunable black phosphorus plasmonic nanoribbon Salisbury screen device, scanning electron microscope image of nanoribbons, and simulation results for absorption modulation and electric field intensity profile. .......................................................... 62

6.3 Experimental armchair axis absorption modulation results and dark field optical microscope image of a completed nanoribbon Salisbury screen device........................................................................64

6.4 Device and experimental setup schematic for proposed investigation of spin-plasmon excitations in bismuth antimony telluride ...............69

# Chapter 1

## Introduction

## 1.1 The Case for Active Nanophotonics

The National Research Council defines nanophotonics as "the science and engineering of light matter interactions that take place on wavelength and subwavelength scales where the physical, chemical or structural nature of natural or artificial nanostructured matter controls the interactions."[1] The field of nanophotonics as a whole has seen dramatic growth over the past few decades, as evidenced by papers published or technological impact. Examples of the latter that are already established include integrated photonics for on-chip optical communications; plasmonic, heat-assisted magnetic recording of data; nano-scale imaging; advanced photovoltaic devices; miniaturized optoelectronic components, including LEDs and lasers; and, a range of chemical and biological sensors.

While the nanophotonics community has generated a multitude of complex structures and mechanisms to control light at the nanoscale, the large majority are static. In the field of metamaterials and metasurfaces – artificial optical materials composed of subwavelength structural elements – for example, it is now possible to replicate nearly all of the optical functionality of bulk optics, and more, in compact, flat structures.[2-5] Two such examples are shown in Figure 1.1. However, once a structure is designed and fabricated to achieve a given absorption, emission or luminescence response, this behavior is fixed. To achieve truly complete control of radiation, we need to develop active nanophotonic structures that can control the amplitude, phase, and polarization of light, all as a function of time.

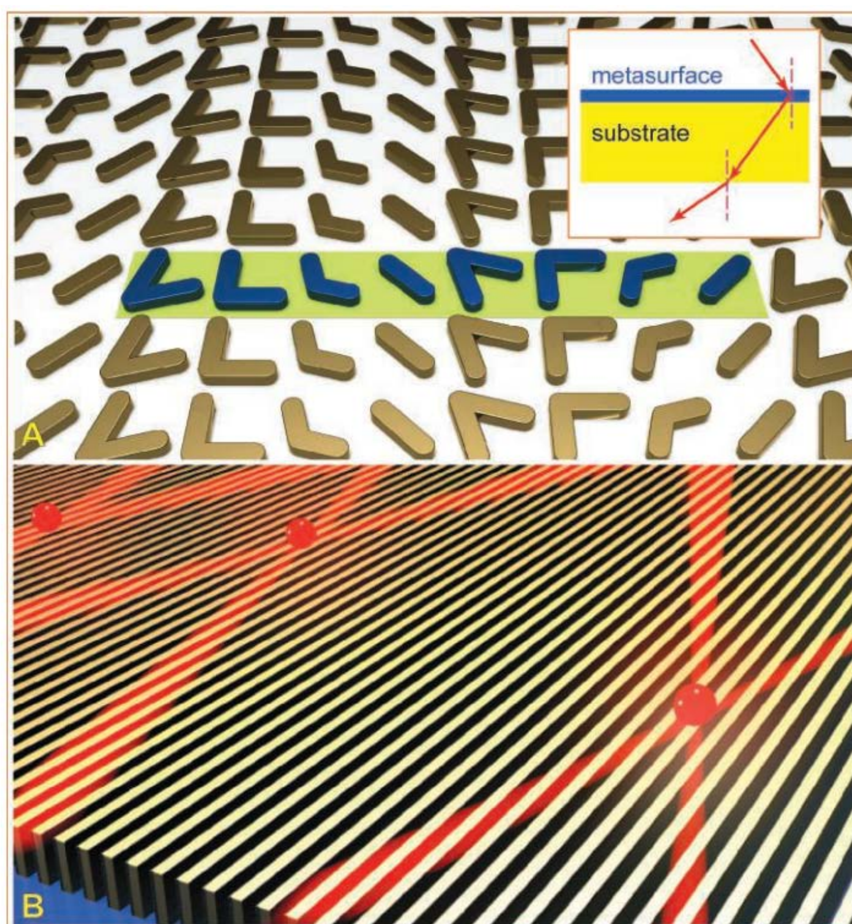


**Figure 1.1:** Static metasurfaces. **a)** A nano-antenna array plasmonic metasurface consisting of blocks of v-shaped gold nanostructures that exhibits negative refraction and b) A hyperbolic metasurface consisting of a thin metallic grating on a dielectric substrate designed to enhance the emission rate of quantum emitters. Reproduced from Reference 5.

If dynamic, tunable control of the near and far-field propagation of light can be achieved in real time, a number of promising applications may be expected to emerge. Electrically tunable metasurface optical phased arrays could enable beam steering for high-speed, solid-state lidar detectors. Other technology directions for active metasurfaces include holographic displays for virtual and augmented reality, LED lighting wi-fi (li-fi), and active thermal radiation management. Beyond metamaterials, new devices and materials for high-speed optical modulation could revolutionize telecommunications for both long and short-haul distances. In the long run, it might be possible to use such techniques to replace electrical

interconnects in and around electronic microprocessors, or even to usher in entirely new, all-optical computing paradigms.[6, 7]

While several paradigms have been posed for dynamically tunable optical materials, electrical tuning promises uniquely compelling advantages in speed, reliability and cost. Phase changes materials, for example, can generate large tunability in the refractive index, but suffer from slow switching speeds, hysteresis, and low reliability. Likewise, thermal effects can be utilized in CMOS materials, but are slow as well, and are typically difficult to miniaturize due to problems with cross-talk. Semiconductor charge injection can occur at gigahertz speeds, and field-based effects like the Stark shifting of semiconductor quantum wells can be even faster. Thus, the research and development of ideal, electrically tunable optical materials is critical to the viability of these technologies.

## 1.2 Van der Waals Materials

Van der Waals materials are two-dimensional crystals that stack together in sheets, adhered only by van der Waals interactions.[8] The two-dimensional nature of these layers has a number of important impacts on their electronic, optical, mechanical and thermal properties. For example, the band structure of graphene, the most studied van der Waals material, is radically different than that of graphite, its bulk form. The unique electronic landscapes in these materials may be thought of as deriving from quantum confinement, and precipitate a range of novel optoelectronic phenomena.[9]

The family of explored van der Waals materials is growing rapidly, and now includes insulators, metals and semiconductors with light-matter interactions that span the electromagnetic energy spectrum, as depicted in Figure 1.2. Most importantly for electrically-tunable nanophotonics, the ultra-thin geometry of van der Waals materials enables efficient modification of their optical properties via field-effect gating and other electro-optical effects.

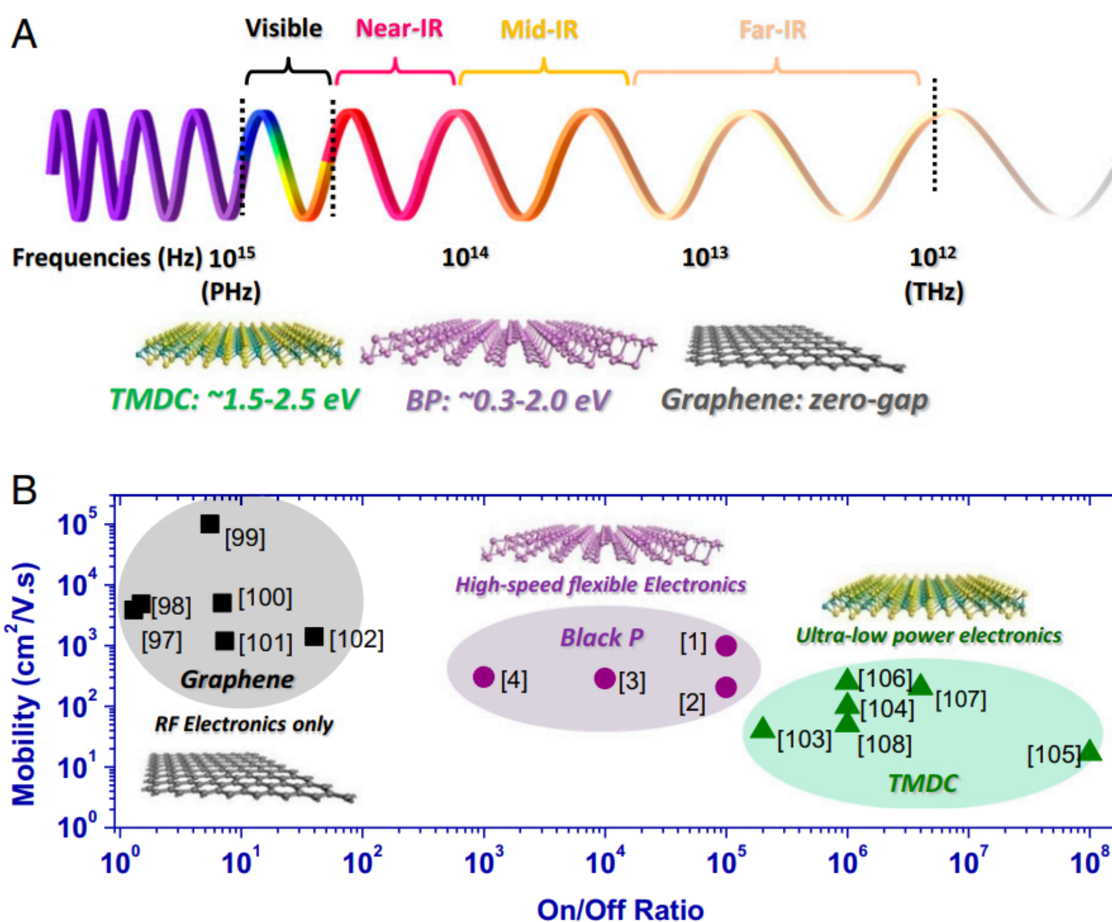


**Figure 1.2:** The family of van der Waals materials spans **a)** light-matter interactions across the electromagnetic spectrum and **b)** a range of mobility and on / off ratio values. Reproduced from Reference 10.

The electro-optical responses of a small number of two-dimensional materials have already been explored. In graphene, for example, a plasmonic response can be generated and modulated at mid to far-infrared frequencies by adding electrons or holes via field-effect gating.[11] At near-infrared frequencies, gating allows Paul-blocking of interband optical transitions, wherein filling or depleting the electronic states associated with these transitions shuts them off or turns them on.[12] In other two-dimensional materials, strongly bound excitons generate strong light-matter interactions in the visible and near-infrared that can be tuned electrically. In the transition metal dichalcogenides, for example, large refractive index

tunability can be achieved near a dominant visible frequency exciton peak by broadening the spectral width of this peak via charge injection.

Black phosphorus is a new and compelling candidate for van der Waals optoelectronics. This layered, semiconducting allotrope of phosphorus, evolves continuously from a bulk-like semiconductor to a natural quantum well structure when thinned down to the few-layer limit. As the layer count is reduced, quantum confinement increases the band gap from 0.3 eV in bulk to approximately 2 eV for monolayers.[10] In this regime, few layer black phosphorus may be expected to exhibit tunable optoelectronic behavior along the lines of that seen in compound semiconductor quantum well structures, which are ideal amplitude and phase modulators. In addition, the anisotropic crystal structure of black phosphorus induces severe anisotropy in its electronic, thermal, and optical properties.[10] This anisotropy opens the door for compelling new physics, such as hyperbolic plasmons, and technology applications, such as polarization control and beam-steering of propagating surface waves.

As the family of van der Waals materials expands, we can hope to both shed light on novel physics, and develop a new toolbox for dynamic nanophotonics and optoelectronics that will enable new technology.

### 1.3 Topological Materials

Topological materials, and specifically topological insulators, are a second class of promising new materials for active nanophotonics. Three-dimensional electronic topological insulators are band insulators with Dirac semimetallic surface states in which carrier spins are locked in plane, orthogonal to their crystal momentum.[13, 14] These surface states are remarkably robust; they span the entire bulk band gap, and are topologically protected against material defects and reconstructions that do not break time reversal symmetry.[15] In addition, back-scattering events – in which both momentum and spin directions must flip – are strongly suppressed. Many of these compounds, such as the bismuth and antimony chalcogenides, are also van der Waals materials.

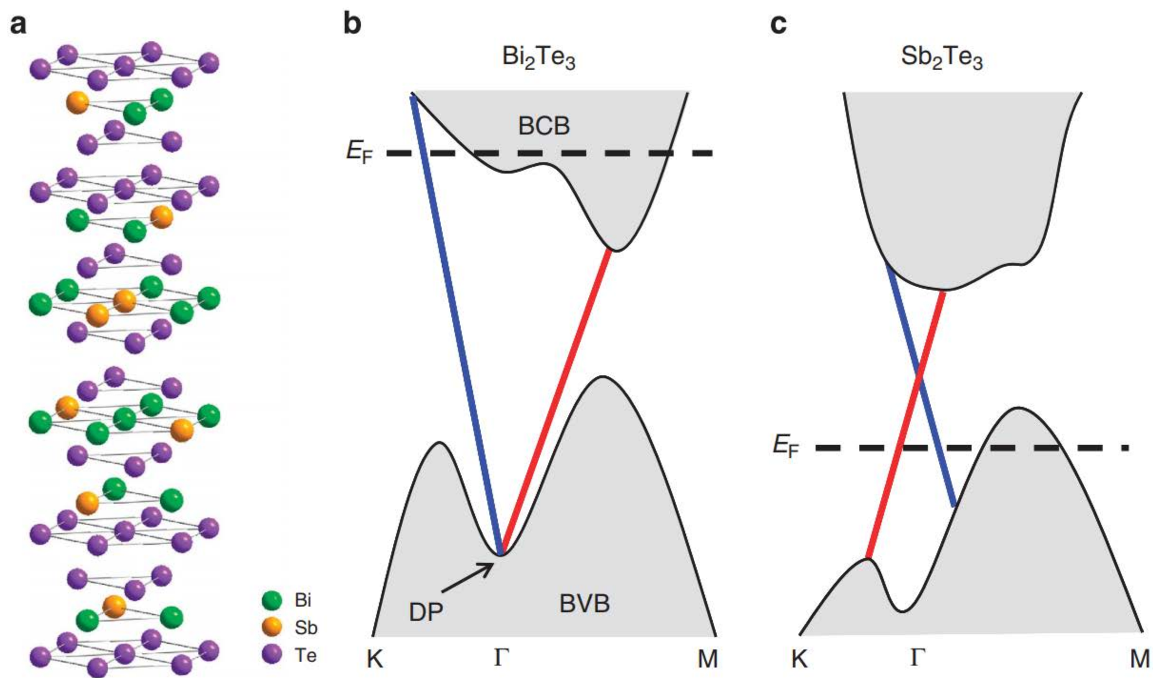


**Figure 1.3: a)** The van der Waals crystal structure of bismuth antimony telluride, and **b), c)** the electronic band structures of bismuth telluride and antimony telluride, respectively. The two spin-polarized surface state bands, which intersect at the Dirac point, are shown in blue and red. Reproduced from Reference 16.

Over the last decade, a range of new electronic phenomena have been observed in topological insulator systems, including the quantum anomalous Hall effect.[17] These materials have also been predicted to host physically and technologically compelling optical and optoelectronic behavior. Some of these effects have been experimentally demonstrated – giant magneto-optical effects, helicity-dependent photocurrents and more – but many other remarkable and novel light-matter interactions, including gapless infrared photodetection, gate-tunable, long-lived Dirac plasmons, and hybrid spin-plasmon modes, remain to be seen and explored.[18-22]

Plasmonics is one promising direction for electrically tunable optoelectronics in topological insulators. Due to the suppression of carrier back scattering, plasmon resonances are expected to exhibit reduced dissipation and enhanced lifetimes. In addition, spin-momentum locking is predicted to hybridize they typical charge degree of freedom with spin, yielding hybrid spin-plasmon modes. In theory, in thin topological insulator films this hybridization

can be tuned from purely charge-like excitations to purely spin-like excitations by changing the carrier densities on the top and bottom surfaces via field-effect gating.

A second exciting direction is the electrical control of surface and bulk interband and intraband optical transitions in topological insulators via field-effect gating. These four types of optical transitions can in principle all be modulated, much like Paul-blocking and free carrier effects in graphene. By controlling these interactions, topological insulators could enable efficient optical modulation, tunable coupling to spintronic systems, or other paradigms yet to be explored.

While topological insulator optoelectronics is an area ripe with opportunity, materials challenges persist. To see these concepts to fruition, ideal materials must be developed that exhibit strong light matter interactions with the topological surface states, and weak bulk carrier interactions.

### 1.4 The Scope of this Thesis

This thesis explores novel light-matter interactions in quantum materials, and how such phenomena may be applied for active nanophotonics.

Chapters 2 and 3 of this thesis focus on new optoelectronic phenomena in few-layer black phosphorus. In Chapter 2, we demonstrate the Pauli-blocking of intersubband optical transitions in black phosphorus quantum wells under carrier injection. In Chapter 3, we demonstrate the quantum-confined Stark effect in black phosphorus, and examine the role of anisotropy in black phosphorus electro-optics. We further explore how anisotropic electro-optical effects in few-layer black phosphorus yield tunable birefringence and dichroism.

Chapter 4 of this thesis focuses on optical transitions in bismuth antimony telluride topological insulator materials. We demonstrate electrical control of bulk interband transitions, and both topological surface and bulk intraband transitions. We construct a permittivity and transfer matrix model of this behavior. We also seek to observe topological

surface interband transitions, and develop a method for epitaxial lift-off of bismuth antimony telluride films from common epitaxy substrates.

Chapter 5 of this thesis reports theory results indicating that resonant nanophotonic devices loaded with few-layer black phosphorus can act as ideal, polarization-dependent phase and amplitude modulators with highly efficient performance. This chapter serves as an example application of the fundamental research described in Chapters 2 through 4, and highlights an important direction for future work.

Chapter 6 of this thesis reports existing results and immediate plans for ongoing work, and provides a perspective on future directions. First, we describe initial results from an ongoing effort to observe gate-tunable, anisotropic plasmon resonances in black phosphorus nanoribbon structures. Next, we propose a program of experiments to follow up on the theory results from Chapter 5. We further propose a direction for future experiments on hybrid spin-plasmon modes in topological insulator materials. Lastly, we provide a perspective on both the work described herein, and the scientific and technological impact we might expect from future research on electrically tunable light matter interactions in quantum materials.

Experimental methods are detailed in the Appendix.

# Chapter 2

# Charge-Driven Modulation of Intersubband Optical Transitions in Few-Layer Black Phosphorus

Here, we report measurements of the infrared optical response of thin black phosphorus under field-effect modulation.[23] We interpret the observed spectral changes as a combination of an ambipolar Burstein-Moss (BM) shift of the absorption edge due to band-filling under gate control, and a quantum confined Franz-Keldysh (QCFK) effect, phenomena which have been proposed theoretically to occur for black phosphorus under an applied electric field. Distinct optical responses are observed depending on the flake thickness and starting carrier concentration. Transmission extinction modulation amplitudes of more than two percent are observed, suggesting the potential for use of black phosphorus as an active material in mid-infrared optoelectronic modulator applications.

## 2.1 Introduction

The emergence of a variety of two-dimensional materials has spurred tremendous research activity in the field of optoelectronics[24-27]. While gapless graphene can in principle exhibit an optoelectronic response at wavelengths ranging from the far infrared to the ultraviolet, its optoelectronic behavior is limited by a lack of resonant absorption and poor optical modulation in the absence of one-dimensional confinement. On the other hand, the semiconducting molybdenum- and tungsten-based transition metal dichalcogenides have shown considerable prospects for visible frequency optoelectronics. Yet while these materials promise exciting new directions for optoelectronics and nanophotonics in the visible range, they have limited response for lower energy, infrared light.

The isolation of atomically thin black phosphorus in recent years has bridged the wavelength gap between graphene and transition metal dichalcogenides, as black phosphorus is an emerging two-dimensional semiconductor material with an infrared energy gap and typical carrier mobilities between those of graphene and transition metal dichalcogenides.[28-32] Since the first isolation of black phosphorus and demonstration of a field effect device, numerous reports investigating the synthesis and optoelectronic properties of this material have emerged, appropriately summarized in recent reviews.[10, 28, 29, 33, 34] Likewise a number of reports have also appeared on the applications of black phosphorus in fast photodetectors[35], polarization sensitive detectors,[36] waveguide integrated devices[37], multispectral

photodetectors[38], visible to near-infrared absorbers[39] and emitters, [40-43]heterojunction[30] and split gate p-n homojunction photovoltaics[44], gate-tunable van der Waals heterojunctions for digital logic circuits[45, 46] and gigahertz frequency transistors in analog electronics[47]. A majority of the studies on both the fundamental optical properties of black phosphorus and applications in optoelectronic devices have explored only the visible frequency range[48-51]. Therefore, little is known about the intrinsic optical response of black phosphorus in the infrared range. As a narrow band-gap semiconductor, much of the potential for black phosphorus lies in these infrared optoelectronic applications – ranging from tunable infrared emitters[52] and absorbers for waste heat management/recovery[53] to thermophotovoltaics[54] and optical modulators for telecommunications[55]. Theoretical investigations of black phosphorus have suggested novel infrared optical phenomena, such as anisotropic plasmons[56, 57], field-effect tunable exciton stark shifts[58], and strong Burstein-Moss[59] and quantum-confined Franz-Keldysh effects[60] that promise to open new directions for both fundamental nanophotonics research and applications. In this work, we report the first experimental observations of the infrared optical response of ultrathin BP samples under field effect modulation. We observe modulation of oscillations in the transmission spectra which we attribute to a combination of an ambipolar Burstein-Moss shift / Pauli-blocking effect and quantum-confined Franz-Keldysh behavior.

## 2.2 Experimental Measurements of the Black Phosphorus Optical Response with Doping by an Electrostatic Gate

Measurements were performed on black phosphorous flakes that were mechanically exfoliated in a glove box onto a 285 nm $SiO_2$/Si substrate. We analyzed three flakes of 6.5 nm, 7 nm, and 14 nm thickness, determined by Atomic Force Microscopy (details are provided in the Supporting Information Fig. S6), and lateral dimensions of approximately 10 μm x 10 μm. A schematic of our experimental setup is shown in Figure 1a. Standard electron beam lithography and metal deposition methods were used to define Ni/Au electrodes to each exfoliated BP flake. The samples were then immediately coated in 90nm PMMA for protection against environmental degradation. Once encapsulated in PMMA we observe minimum degradation of our samples to ambient exposure as verified by Raman

spectroscopy[61] and reported in literature precedent[62]. Transmission measurements were obtained via Fourier Transform Infrared (FTIR) Spectroscopy. All optical measurements were done in a Linkam cryo-stage at a pressure of 3 mTorr and a temperature of 80 K. First, a room-temperature gate-dependent source-drain current was measured to extract approximate carrier densities as a function of gate bias. Transmission spectra were then gathered at different gate voltages applied between the flake and lightly doped Si substrate. We note that in our setup, the silicon substrate is grounded and BP experiences the applied voltage, so the sign of the applied voltages is reversed from the more common convention. In order to probe the electric field- and charge-carrier-dependent optical properties of the BP, all spectra were normalized to the zero-bias spectrum. The measured infrared optical properties result primarily from the unique band structure of thin BP, schematically depicted in Figure 1b. Quantized inter sub-band transitions provide the primary contribution to its zero-field optical conductivity.

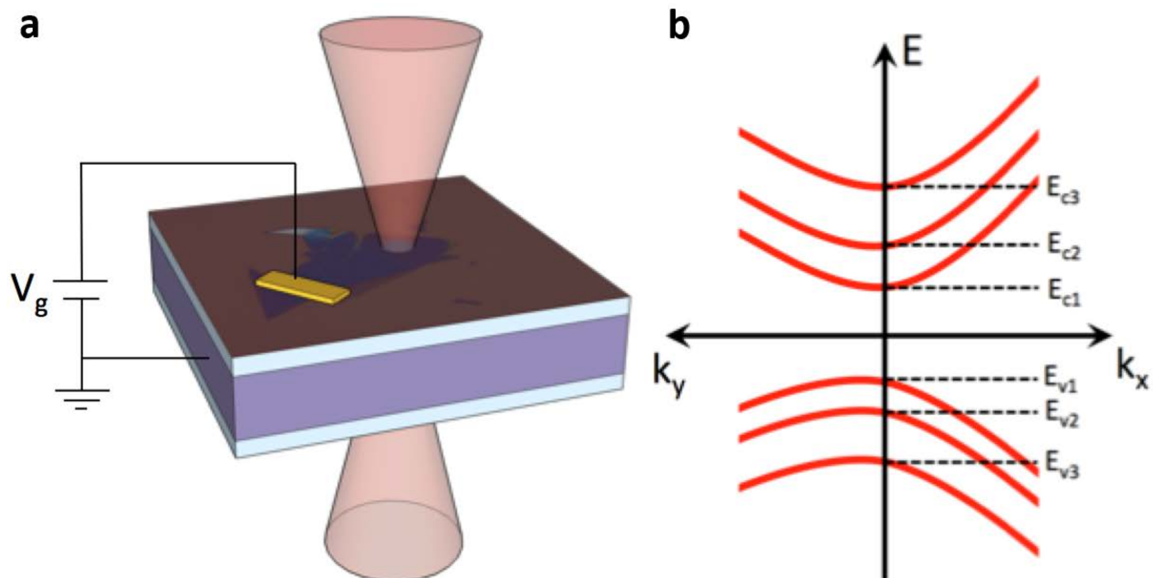


**Figure 2.1: a)** Schematic illustration of transmission modulation experiment. Broadband mid-IR beam is transmitted through black phosphorus sample. Variable gate voltage applied across $SiO_2$ modulates transmission extinction, **b)** Schematic band diagram of few-layer black phosphorus with subbands arising from vertical confinement.

### 2.2.1 7 nm Flake with Light Doping

We first present results for the 7 nm thick BP flake, in Figure 2. An optical image is shown in Figure 2e. FTIR spectra were taken using a Thermo Electron iS50 FTIR spectrometer and Continuum microscope for which the light source is a broadband, unpolarized tungsten glo-bar. To improve signal/noise and minimize spatial drift, we surrounded the sample with a 150 nm thick gold reflector which also served as the gate electrode. The extinction modulation results are presented in Figure 2a. We observe two major features in this flake at energies of 0.5 eV (I) and 0.9 eV (II). The dip in extinction at 0.5 eV is present for both positive and negative gate voltages, as the sample is increasingly hole or electron doped, respectively. It grows in strength as the doping is further increased at larger gate-biases. The same trend is true for the feature at 0.9 eV, where a smaller peak in extinction modulation is observed for both polarities of voltage. This peak also is strengthened as the gate voltage is increased to +/- 120V. To gain insights into this behavior, we measure gate-dependent transport, using a scheme in which a positive bias induces hole-doping, and a negative bias introduces electron-doping. We observe ambipolar transport at room temperature and atmospheric conditions, as shown in Figure 2b. Similar results have been shown in the literature with on/off ratios of ~$10^4$ for flakes thinner than the one considered here, at low temperature.[30, 63] From this, the CNP is observed to be at 20 V, and, using the parallel plate model described in the Supporting Information, the unbiased, n-type carrier concentration is estimated to be $1.5\cdot10^{12}$ $cm^{-2}$. Further discussion on the depletion length and vertical charge distribution within the flake has been provided in the Supporting Information Figure S5.

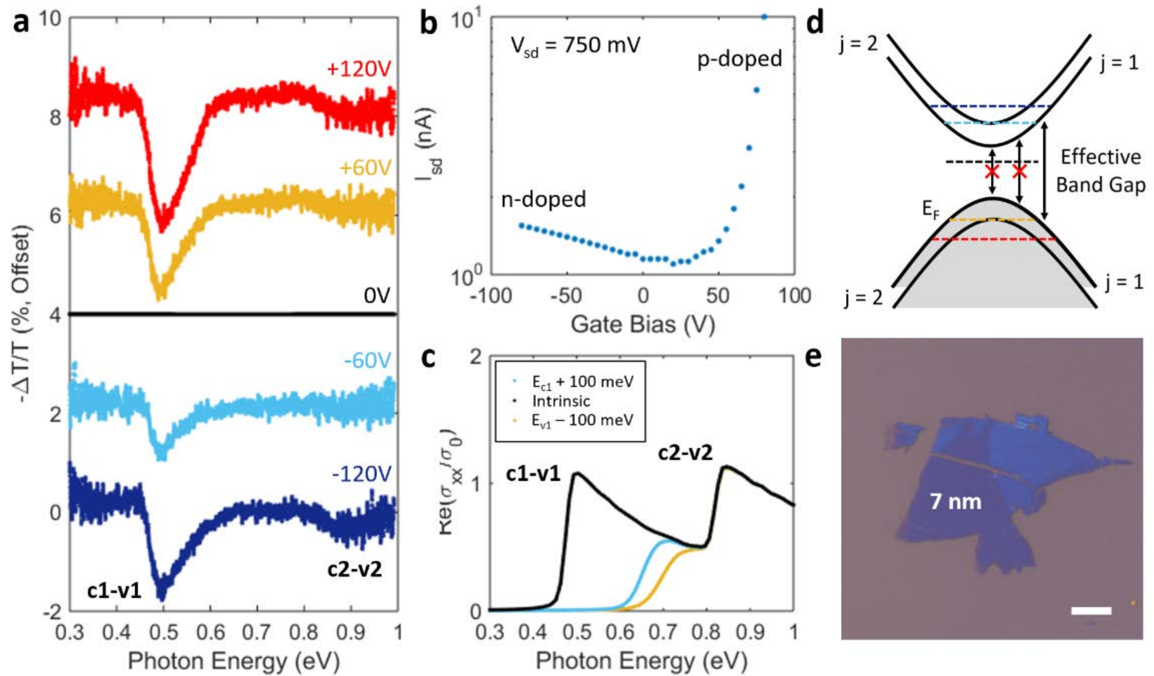


**Figure 2.2:** Gate modulation of lightly doped 7 nm flake. **a)** FTIR transmission extinction vs photon energy normalized to zero bias **b)** Source-drain current vs gate voltage. Ambipolar conduction is seen. **c)** Calculated optical conductivity of a 4.5 nm thick BP flake at different carrier concentrations, normalized to the universal conductivity of graphene. No field effects included. **d)** Schematic of electronic band structure and allowed interband transitions at different voltages. **e)** Optical microscope image of flake. Scale bar is 10μm.

We can interpret our spectroscopic results with consideration of a Burstein-Moss shift, which is a well-known phenomenon in chemically doped narrow-band gap semiconductor materials. This effect, which changes the optical band gap of a semiconductor, results from band-filling or Pauli-blocking. As the charge carrier density is increased and the Fermi level moves into the conduction or valence band, there are fewer unoccupied electronic states available, and optical transitions to the occupied states are disallowed. This results in a decrease in the optical conductivity of the material at the energy of the transition, and is manifest in measurements as a decrease in absorption.[64, 65] Because this flake exhibits ambipolar transport behavior, we can explain both features (I) and (II) as arising from an ambipolar BM effect. At zero applied bias, the flake is very lightly doped, and all optical transitions are allowed. As a positive gate voltage is applied and the sample becomes hole doped, lower energy optical transitions become disallowed and the absorption of the flake

decreases. Feature (I) corresponds to the Pauli-blocking of the $E_{11}$ intersubband transition, and feature (II) corresponds to the blocking of the $E_{22}$ intersubband transition, shown schematically in Figure 2d. For a negative gate voltage, as the sample is electron-doped and the Fermi level moves into the conduction band, the $E_{11}$ and $E_{22}$ transitions are again blocked due to band filling, resulting again in a decrease in absorption. To support this explanation, we calculate the optical conductivity for the flake, as shown in Figure 2c to identify the appropriate energies of the intersubband transitions. To do so, we use the Kubo method described by Tony Low, et al.[59], to calculate the components $\sigma_{\alpha\beta}$ of the optical conductivity tensor. Further details on the Hamiltonian, eigenfunctions and eigenvalues, velocity operator and more are available in that reference, and Matlab code used to perform the calculation is available in the Appendix.

$$\sigma_{\alpha\beta}(\boldsymbol{q},\omega) = -i\frac{g_s\hbar e^2}{(2\pi)^2}\sum_{ss'jj'}\int d\boldsymbol{k}\,\frac{f(E_{sj\boldsymbol{k}}) - f(E_{s'j'\boldsymbol{k}'})}{E_{sj\boldsymbol{k}} - E_{s'j'\boldsymbol{k}'}} \times \frac{\langle\Phi_{sj\boldsymbol{k}}|\hat{v}_\alpha|\Phi_{s'j'\boldsymbol{k}'}\rangle\langle\Phi_{s'j'\boldsymbol{k}'}|\hat{v}_\beta|\Phi_{sj\boldsymbol{k}}\rangle}{E_{sj\boldsymbol{k}} - E_{s'j'\boldsymbol{k}'} + \hbar\omega + i\eta} \qquad (2.1)$$

We note that this optical conductivity is normalized to $\sigma_0 = e^2/4\hbar$, the universal optical conductivity of graphene. It can then be used to calculate the (non-normalized) dielectric function, using the static dielectric constant $\epsilon_{rel}$ and black phosphorus thickness $\Delta$.

$$\epsilon_{jj}(\omega) = \epsilon_{rel} + i\frac{e^2}{4\hbar}\frac{\sigma_{jj}(\omega)}{\Delta\epsilon_0\omega} \qquad (2.2)$$

The observed transitions energies are consistent with theoretical models that predict an increase in band gap energy from the bulk 0.3 eV value as the material thickness decreases to several layers or less.[50] This deviation from the bulk band gap indicates the influence of vertical confinement of charge carriers, a feature of the two-dimensionality of the material. We note that these transition energies suggest that the true thickness of our sample is thinner than 7 nm, at approximately 4.5 nm. This apparent variation between true and observed thickness from AFM topography is a result of surface oxidation, as has been recently

reported.[66] The surface oxide on our samples is expected to be between 1-2 nm on either side, which appears inevitable despite following best practices, and is stable with no measurable degradation over an ambient exposure of > 18 hrs in ambient (see Supporting Information). It is noteworthy that we observe extinction modulation at relatively high photon energies, indicative of very large charge modulation taking place in the fraction of the BP nearest to the silicon oxide interface, with an accumulation/depletion layer that decays over the remainder of the flake. This is consistent with in-depth calculations of charge screening in BP using the Thomas-Fermi model done previously, reported by Tony Low, et al.[56] We estimate this screening length to be of order 3 nm for our devices in the Supporting Information. This ambipolar, gate-modulated Burstein-Moss shift is the first observed in a two-dimensional semiconductor, to the best of our knowledge.

### 2.2.2 14 nm Flake with Light Doping

We next present data for a BP flake of 14 nm thickness in Figure 3. An optical image is shown in Figure 3e. Extinction measurements are again taken with an iS50 FTIR spectrometer and Continuum microscope for which the light source is a tungsten glowbar. These results are presented in Figure 3a. Four prominent features are observed to modulate under application of a gate voltage, at energies of 0.35 eV, 0.41 eV, 0.55 eV, and 0.75 eV. As in the previous sample, they grow in strength with increased magnitude of the gate voltage, regardless of polarity. To better understand this behavior, we again measure gate-dependent transport, reported in Figure 4b. We observe ambipolar transport characteristics as in the previous flake, centered about a conductance minimum at approximately 20 V. Again using a parallel-plate capacitor model, we estimate an unbiased n-type carrier density of $1.5 \cdot 10^{12}$ cm$^{-2}$ for a 20 V CNP.

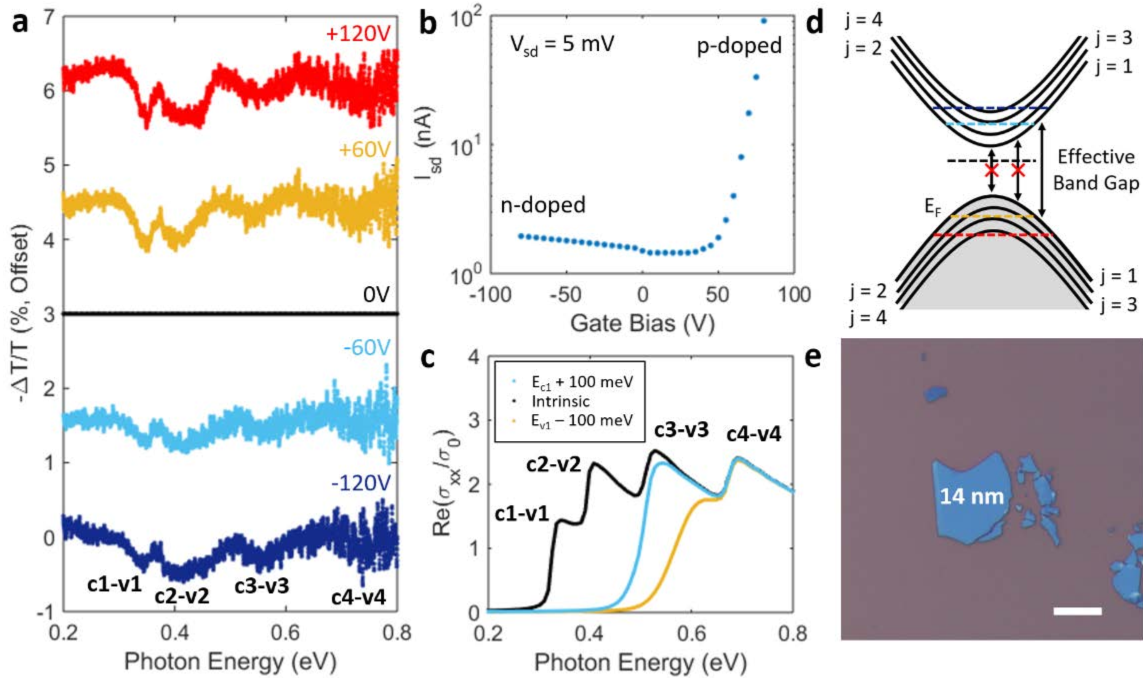


**Figure 2.3:** Gate modulation of lightly doped 14 nm flake. **a)** FTIR transmission extinction vs photon energy normalized to zero bias **b)** Source-drain current vs gate voltage. Ambipolar conduction is seen. **c)** Calculated optical conductivity of a 10 nm thick BP flake at different carrier concentrations, normalized to the universal conductivity of graphene. No field effects included. **d)** Schematic of electronic band structure and allowed interband transitions at different voltages. **e)** Optical microscope image of flake. Scale bar is 10 µm.

We propose that the optical modulation for this sample also results from an ambipolar Burstein-Moss effect. In this case, as the Fermi energy is moved into the conduction band of the BP under negative bias, transitions become disallowed and the transmission is increased at each of the $E_{11} - E_{44}$ energies. Under positive bias, as the Fermi energy is moved into the valence band, the band-filling effect of opposite charge carrier type results in negative extinction modulation peaks at the same energies of transitions $E_{11} - E_{44}$. As in the previous sample, we estimate an oxide layer of 1-2 nm has grown on our BP on either surface. Based on optical conductivity calculations presented in Figure 3c, we again estimate the adjusted thickness of our flake to be less than that measured by AFM, at approximately 10 nm. We further note that for this sample, the measurement extended beyond the area of the flake, to cover the flake and an area of bare silicon oxide roughly eight times the flake are.

We thus suggest that the true modulation strength of this device is of order six percent, not the 0.75 percent indicated by the modulation of the entire area.

### 2.2.3 6.5 nm Flake with Heavy Doping

Finally, results for the 6.5 nm thick flake are reported in Figure 4, for which an optical image is shown in Figure 4e. Unlike the previous two flakes, transmission measurements for this sample were taken using a Nicolet Magna 760 FTIR spectrometer coupled to a Nic-Plan infrared microscope on infrared Beamline 1.4.3 at the Advanced Light Source (ALS) at Lawrence Berkeley National Laboratory. This allowed us to perform measurements using a high brightness, diffraction-limited infrared beam, which is beneficial for accurately analyzing the small-area BP samples attainable by mechanical exfoliation. In contrast to the previous measurements, the incident light was elliptically polarized due to the synchrotron source, with an intensity ratio of two to one. The major axis and details of the polarization state are indicated and discussed in Supporting Information Figure S3.

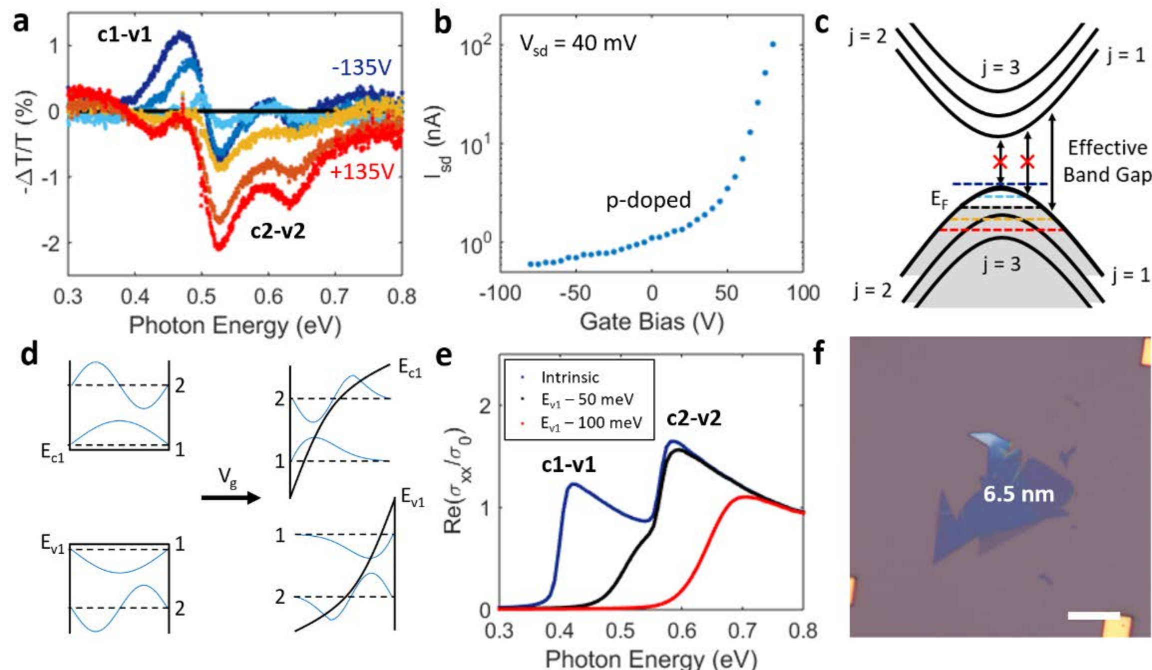


**Figure 2.4:** Gate modulation of a heavily doped 6.5 nm flake. **a)** FTIR transmission extinction vs photon energy normalized to zero bias **b)** Source-drain current vs gate voltage. Only hole-type conduction is seen. **c)** Schematic of electronic band structure and

allowed interband transitions at different voltages. **d)** Schematic representation of quantum confined Franz-Keldysh Effect **e)** Calculated optical conductivity of a 6.5 nm thick BP flake at different carrier concentrations, normalized to the universal conductivity of graphene. No field effects included **f)** Optical microscope image of flake. Scale bar is 10 μp.

Figure 4a shows the primary result of this experiment, which is the modulated extinction of the sample at different voltages, normalized to the zero-bias extinction spectrum. Three prominent features are observed in these spectra. First, under negative applied bias (i.e.: when the sample is being depleted of holes), a negative peak (I) appears in transmission near 0.45 eV, which grows in amplitude and broadens to lower energies as the magnitude of the bias increases. Second, under positive applied bias (i.e.: when the sample is being increasingly hole-doped), a positive peak (II) appears in transmittance near 0.5-0.7 eV. Lastly, these two effects, which we propose to depend on the Fermi level, are superimposed with an oscillatory feature (III) that varies with the magnitude of the applied field, but not its polarity, and which is most clearly visible in the negative bias spectra in the 0.5 - 0.7 eV range.

To better understand these results, transport measurements were again taken at room temperature under ambient conditions, as shown in Figure 4b. The gate dependence of the conductance indicates that, unlike the previous samples, this BP flake was initially heavily hole-doped, as ambipolar transport is not observed and only hole-type conduction is seen even at large negative bias. This indicates a zero-bias carrier concentration in excess of $6{\cdot}10^{12}$ $cm^{-2}$.

Due to the distinct character of each feature and their relation to the transport measurements, we can understand the overall spectral shifts as arising from a combination of a Burstein-Moss (BM) shift and a quantum confined Franz-Keldysh (QCFK) effect, both of which have been predicted theoretically for gated BP flakes of this thickness.[60] In the bulk limit, the Franz-Keldysh effect refers to electron and hole wavefunctions leaking into the band gap, as described by Airy functions. This behavior introduces oscillatory features to the interband absorption spectrum, and redshifts the band edge. In confined systems, the quantum-confined Franz-Keldysh effect similarly modulates intersubband transitions.[67] As

confinement becomes stronger and excitonic effects dominate, this phenomenon eventually gives way to the quantum-confined Stark effect. Because our flake exceeds a thickness of ~4 nm, we expect excitonic effects to be weak and therefore will not focus our discussion on the quantum-confined Stark effect or a normal-to-topological phase transition in our analysis.[50, 51, 58]

We suggest that peak (I) at 0.45 eV can be described by the onset of j = 1 intersubband transitions as the material is depleted of holes at negative gate voltages and the valence band is un-filled, in agreement with our transport measurements. We further suggest that peak (II) can be described primarily by the suppression of j = 2 inter sub-band transitions as more holes are accumulated in the flake at positive gate voltages. This behavior is shown schematically in Figure 4d, and is again supported by calculations of the optical conductivity of the flake for various doping levels, shown in Figure 4e. Our experimental results correspond to modulation of the calculated intersubband transitions only in part, suggesting that a simple Burstein-Moss shift is insufficient to explain this measurement. From these results, we assign the band gap energy of our flake to be approximately 0.4 eV. Unlike our previous samples, the optical data indicates minimal oxide formation, as the $E_{11}$ and $E_{22}$ transition energies match well to theory for a 6.5 nm thick BP quantum well. Given we do not see the charge neutral point in transport, we do not assign a carrier density to this flake, but can say that with a charge neutral point of greater than -80 V, its p-type carrier density must be greater than $6 \cdot 10^{12}$ cm$^{-2}$.

We suggest that quantum-confined Franz-Keldysh effects lead to the appearance of the additional oscillatory spectral features we observe. Specifically, we point to the oscillations in the negative voltage extinction curves at energies above 0.5 eV – where Burstein-Moss considerations would predict zero modulation – and in the positive voltage extinction curves both in that same range – where Burstein-Moss behavior would predict only a single dip in extinction centered at the 0.575 transition energy – and at 0.45 eV. This oscillatory modulation increases with bias magnitude, but does not depend significantly on the sign of the bias -- behavior which is consistent with shifting of the overlap of the first and second

conduction and valence sub-band wavefunctions, as described by the quantum-confined Franz-Keldysh effect. This behavior is investigated theoretically for gated BP by Charles Lin, et al.[60] In addition, under a sufficiently strong electric field, hybrid optical transitions between sub-bands of different index (eg: $E_{v1}$ to $E_{c2}$) that are nominally forbidden at zero field become allowed. In total, quantum-confined Franz-Keldysh effects in thin BP are expected to lead to behavior including redshifting of intersubband transitions, modification of intersubband selection rules (allowing hybrid transitions), or oscillatory, Airy function modulation of the absorption edge, all of which can be considered as consistent with our experimental observations. However, further theoretical work is needed to understand this effect satisfactorily; the same authors provide evidence in a more recent, experimental report that hybrid transitions may occur with zero applied field as well.[68] Interestingly, we see no evidence of a tunable plasma edge; investigations in the long-wave infrared wavelength range with larger samples would likely be needed to observe this feature.

The clear appearance of the QCFK effect in this measurement distinctly differs from our previous two samples, indicating that BP quantum wells of similar thickness may have very different optical responses. We suggest that the primary reason for this is that this flake is very heavily doped under zero bias, whereas our previous measurements were performed on nearly intrinsic flakes. In particular, in the intrinsic case, field strength and carrier concentration vary proportionally (ie: under larger bias, there is a larger carrier concentration, and vice-versa). To the contrary, in our heavily doped sample, this proportionality is absent, leading to potentially competing effects and the clear emergence of oscillatory features. It is also worth noting that, while we see no clear evidence of the QCFK effect in our first two experiments, it is possible that the large BM shift is simply dominant over the QCFK effect, making the latter effect difficult to observe, or that our increased noise prevents the effect from obviously manifesting. A complete theoretical framework that addresses the interplay between zero-bias carrier concentration and field-effect has not yet been developed, and is beyond the scope of this paper. We also note that, while we see no clear evidence of excitonic effects, and it has been suggested theoretically and experimentally that such effects should

not be present in flakes of this thickness, we do not rule out the possibility that they may be influencing our results.

We note that because of the complicated polarization state of incident light from the synchrotron, and because a previous study has extensively studied this effect experimentally[69], we do not address in detail the anisotropic optical properties of BP. However, due to the primary contribution to the optical conductivity arising from the $\sigma_{xx}$ component, we argue that the only effect of elliptically polarized light is to scale the observed modulation, as discussed in the Supplement Section 1 - 3.

## 2.3 Conclusion

In conclusion, we have demonstrated experimentally that ultra-thin black phosphorus exhibits widely tunable, quantum well-like optical properties at mid-infrared wavelengths. In 7 and 14 nm, lightly doped flakes, we observe for the first time an ambipolar Burstein-Moss shift of intersubband transitions, which also varies with thickness as these transition energies are changed. In a heavily doped 6.5 nm thick BP flake, modulation of infrared transmission takes place as a result of both a Burstein-Moss shift and additional, quantum-confined Franz-Keldysh effects. While our results verify some of the recent theoretical predictions about the electro-optical effects in few-layer BP, they also report new behavior and serve as motivation to further understand the BP optical response as function of sample thickness, doping and field. Our results indicate that BP is both an interesting system for exploring the fundamental behavior of quantum-confined carriers in two-dimensional semiconductors under field-effect modulation, and a promising candidate for tunable mid-infrared optical devices.

# Chapter 3

# Field-Driven Modulation of Absorption and Anisotropy in Few-Layer Black Phosphorus

In this work, we report the first known examples of electrically tunable bifringence and linear dichroism, observed here in few-layer black phosphorus (BP).[70] We observe these effects across mid-infrared and visible frequencies, suggesting that BP is an ideal material system for actively controlling the complex polarization state of light – or even the propagation direction of surface waves. This phenomenon is driven by anisotropic Burstein-Moss (Pauli-blocking) and quantum-confined Stark effects, which we distinguish via different gating schemes, as well as by modification of quantum well selection rules under applied field. We further observe that these effects generate near-unity tuning of BP absorption for certain material thicknesses and photon energies.

## 3.1 Introduction

As photonic structures for controlling the near- and far-field propagation of light become increasingly complex and compact, the need for new materials that can exhibit unique, strong light-matter interactions in the ultra-thin limit is growing rapidly. Ultrathin van der Waals materials are especially promising for such applications, as they allow for the control of light at the atomic scale, and have properties that can be modulated actively using an external gate voltage.[71, 72] Of these, few-layer black phosphorus (BP) is particularly noteworthy due to its high electronic mobility, and a direct band gap that can be tuned as a function of thickness from 0.3 eV to 2 eV.[29, 73] This has enabled the realization of numerous optoelectronic devices with high performance, including photodetectors that can be easily integrated with other photonic elements such as waveguides.[37, 74-77] In addition to this static control, recent works using electrostatic gating and potassium ions have shown that the electronic band gap of BP may be tuned by an electric field.[51, 78-80]

One of the most salient features of BP is its large in-plane structural anisotropy, leading to a polarization-dependent optical response[49, 57, 81] as well as mechanical[82], thermal[83], and electrical transport characteristics[36, 84] that vary with in-plane crystallographic orientation.[31] This optical anisotropy corresponds to a large, broadband birefringence[85], wherein the distinct optical index of refraction along each axis leads to a phase delay

between polarization states of light. Moreover, mirror-symmetry in the x-z plane forbids intersubband optical transitions along the zigzag axis, and as a result, BP exhibits significant linear dichroism, wherein the material absorption depends strongly on the polarization state of exciting light.[81, 86]

In this work, we experimentally demonstrate that the application of a static electric field enables the tunability of the linear dichroism of few-layer black phosphorus (BP). This response – which approaches near-unity tunability of the BP oscillator strength for some thicknesses and photon energies – is achieved by active control of quantum-confined Stark and Burstein-Moss effects, and of quantum-well selection rules. We observe anisotropic tunability from the visible to mid-infrared (mid-IR) spectral regimes, behavior not seen in traditional electro-optic materials such as graphene[87], transparent conducting oxides[88, 89], silicon[90], and quantum wells.[91] This opens up the possibility of realizing novel photonic structures in which linear dichroism in the van der Waals plane can be continuously tuned with low power consumption, because the switching is electrostatic in nature. By controlling optical losses in the propagation plane, for example, efficient in-plane beam steering of surface plasmon polaritons or other guided modes is enabled. Moreover, an electrically tunable polarizer could be realized by modulating the polarization state of light absorbed in a resonant structure containing BP. Because this tunability is strongest at infrared wavelengths, it could also enable control of the polarization state of thermal radiation.[52, 92, 93]

## 3.2 Experimental Measurements of the Black Phosphorus Optical Response with an Applied Electric Field

In order to probe and distinguish the electro-optical tuning mechanisms evident in few-layer BP, we used a combination of gating schemes wherein the BP either floats in an applied field or is contacted, as shown in Fig. 1a and described further in the Methods section. Polarization-dependent optical measurements are taken aligned to the crystal axes, in order to probe the structural anisotropy shown in Fig. 1b. This enables us to isolate the contribution of charge-carrier density effects – i.e. a Burstein-Moss shift – and

external field-effects – i.e.: the quantum-confined Stark effect and control of forbidden transitions in the infrared – to the tunability of linear dichroism, qualitatively illustrated in Figures 1c and 1d.[23, 59, 60, 79] In the anisotropic Burstein-Moss (BM) shift, the optical band gap of the material is changed as a result of band filling and the consequent Pauli-blocking of intersubband transitions. As the carrier concentration of the sample is changed, the Fermi level moves into (out of) the conduction or valence band, resulting in a decrease (increase) of absorptivity due to the disallowing (allowing) of optical transitions.[64, 94] Because intersubband optical transitions are only allowed along the armchair axis of BP, this tunability occurs only for light polarized along this axis. In the quantum-confined Stark Effect, the presence of a strong electric field results in the leaking of electron and hole wave functions into the band gap as Airy functions, red-shifting the intersubband transitions energies.[95] In quantum well structures, this red-shifting is manifested for multiple subbands, and therefore can be observed over a wide range of energies above the band gap. To assess the gate-tunable anisotropy of the optical response of BP, the armchair and zigzag axes, illustrated in Fig. 1b, of the samples considered are identified by a combination of cross-polarized visible microscopy, described in the Supporting Information S1, and either polarization-dependent Raman spectroscopy or infrared measurements, described below. Representative Raman spectra are presented for the visible frequency sample on $SrTiO_3$ in Figure 1e. The optically active armchair axis exhibits a maximum intensity of the $A_g^2$ resonant shift at 465 $cm^{-1}$, whereas this is a minimum for the zigzag axis.[96]

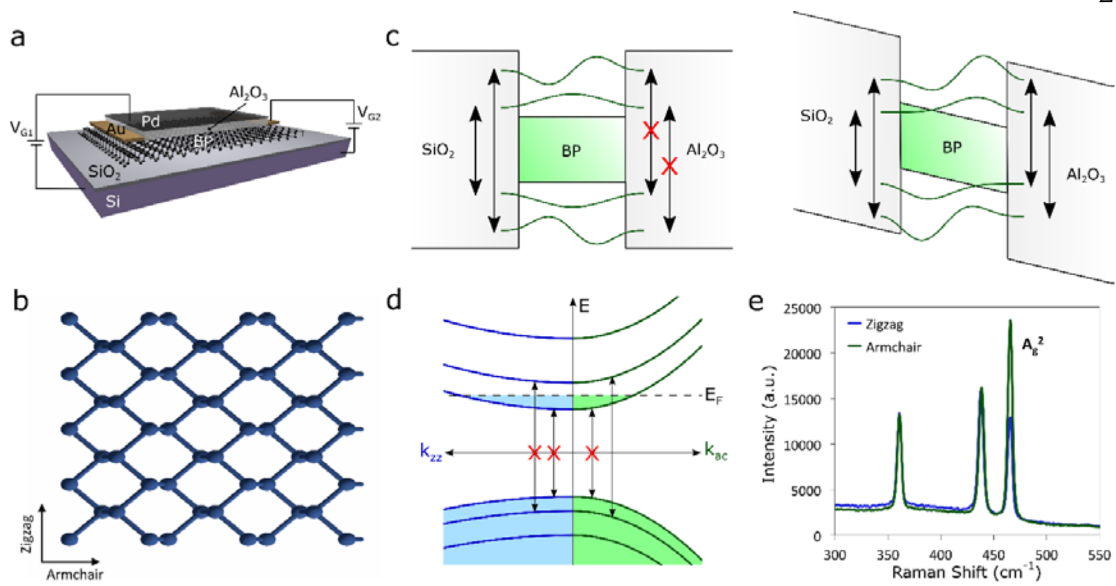


**Figure 3.1.** Anisotropic electro-optical effects in few-layer BP. (a) Schematic figure of infrared tunability devices. Few-layer BP is mechanically exfoliated on 285 nm $SiO_2/Si$ and then capped with 45 nm $Al_2O_3$ by ALD. A semitransparent top contact of 5 nm Pd is used to apply field ($V_{G1}$) while the device floats and 20 nm Ni/200 nm Au contacts are used to gate ($V_{G2}$) the contacted device. (b) Crystal structure of BP with armchair and zigzag axes indicated. (c) Illustration of quantum-confined Stark effect and symmetry-breaking effect of external field. Under zero external field, only optical transitions of equal quantum number are allowed. An external field tilts the quantum well-like energy levels, causing a red-shifting of the optical band gap and allowing previously forbidden transitions. (d) Illustration of anisotropic Burstein-Moss shift in BP. Intersubband transitions are blocked due to the filling of the conduction band. Along the ZZ axis, all optical transitions are disallowed regardless of carrier concentration. (e) Raman spectra with excitation laser polarized along AC and ZZ axes. The strength of the $A_g^2$ peak is used to identify crystal axes.

### 3.2.1 3.5 nm Flake

To illustrate the mechanisms of tunable dichroism of BP in the mid-infrared, we measure tunability of transmittance using Fourier-Transform Infrared (FTIR) microscopy as a function of externally ($V_{G1}$) or directly applied bias ($V_{G2}$), presented for a 3.5 nm thick flake, as determined from atomic force microscopy (AFM) (Figure S1, Supporting Information), in Figure 2. Fig. 2b presents the raw extinction of the flake along the armchair axis at zero bias, obtained by normalizing the armchair axis extinction to that of the optically inactive zigzag axis. A band edge of approximately 0.53 eV is measured,

consistent with a thickness of 3.5nm. A broad, weak shoulder feature is observed at approximately 0.75 eV. The corresponding calculated optical constants for the flake (see Methods for calculation details) are presented in Figure 2c for comparison.

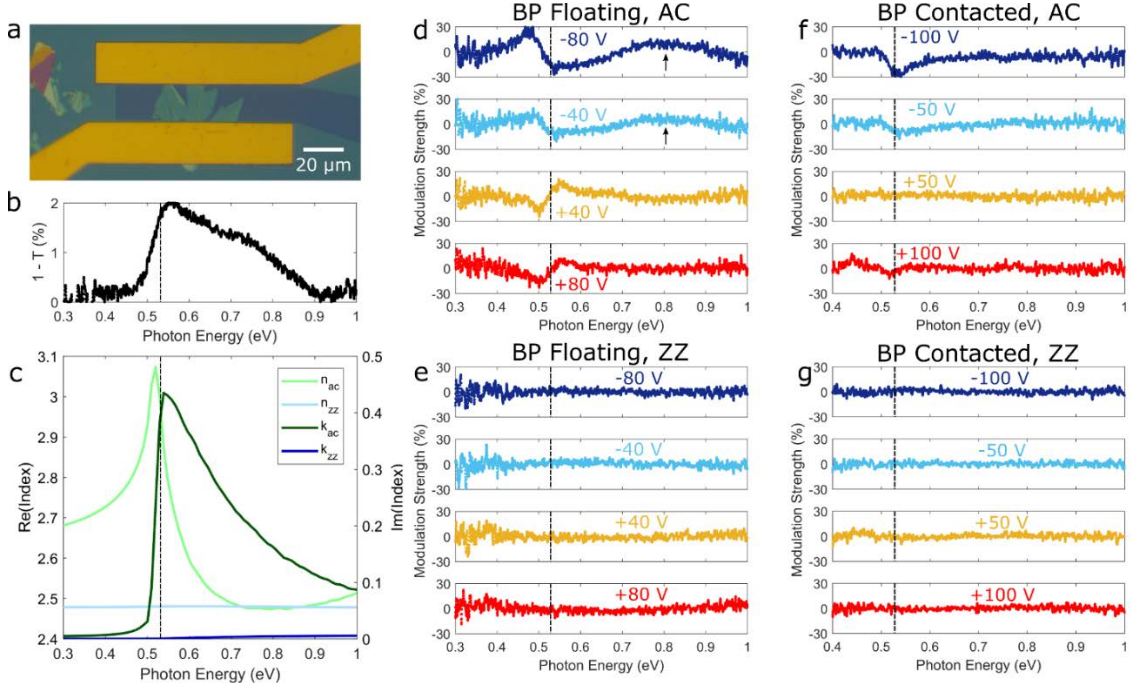


**Figure 3.2.** Electrically tunable linear dichroism: quantum-confined Stark and Burstein-Moss effects and forbidden transitions. (a) Optical image of fabricated sample; (b) Zero-bias infrared extinction of 3.5 nm flake, polarized along armchair (AC) axis. (c) Calculated index of refraction for 3.5 nm thick BP with a Fermi energy at mid-gap. (d) Tunability of BP oscillator strength with field applied to floating device, for light polarized along the AC axis. (e) Corresponding tunability for light polarized along the zigzag (ZZ) axis. (f) Tunability of BP oscillator strength with gating of contacted device, for light polarized along the AC axis. (g) Corresponding tunability for light polarized along the ZZ axis.

Figures 2d and 2e illustrate the influence of an external field on the extinction of BP with carrier concentration held constant (i.e. the BP is left floating). The extinction data for each voltage is normalized to the zero bias case and to the peak BP extinction seen in Figure 2b, to obtain a tuning strength percentage that quantifies the observed tunability of the BP oscillator strength. We note that this normalization scheme underestimates the tuning strength away from the band edge, where BP extinction is maximal. Along the

armchair axis, presented in Fig. 2d, two tunable features are measured near photon energies of 0.5 and 0.8 eV. We explain the first feature at 0.5 eV as arising from a shifting of the BP band edge due to the quantum-confined Stark effect. At negative bias, the band gap effectively shrinks and this is manifest as a redistribution of oscillator strength near the band edge to lower energies. As a result, an increase in absorptance is measured below the zero-bias optical band gap, and a decrease is seen above it. At positive bias, this trend is weakened and reversed. We propose two explanations for this asymmetry: the first is the influence of electrical hysteresis, and the second is the presence of a small internal field in the BP at zero bias, which has been observed in previous works on the infrared optical response of few-layer BP.[81]

The second, higher energy feature observed in the measured spectrum does not correspond to any predicted intersubband transition. Rather, we propose it arises due to the allowing of an optical transition that was previously forbidden by quantum-well selection rule constraints dictated by symmetry (i.e. only transitions of equal quantum number are allowed under zero field[59]). We note that this feature is present in the 0 V extinction spectrum, consistent with a zero-bias internal field. As the symmetry is further broken with an externally-applied electric field, this transition is strengthened. Under positive bias, the internal and external fields are in competition, resulting in minimal change. This suppressed tunability can also be attributed to hysteresis, as before.

In Figure 2e, no tunability is measured for any applied bias for light polarized along the zigzag axis. This can be well understood due to the dependence of the Stark effect on the initial oscillator strength of an optical transition; because no intersubband optical transitions are allowed along this axis, the field effect is weak. Similar behavior has been observed in excitons in $ReS_2$ based on an optical Stark effect.[97] Moreover, while the externally applied field can allow ‘forbidden’ transitions along the armchair axis by breaking the out-of-plane symmetry of the quantum well, in-plane symmetry properties and thus the selection rule precluding all zig-zag axis intersubband transitions are

unaffected. This selection rule and the corresponding symmetry properties have been previously described.[36]

In Figures 2f and 2g, we present the complementary data set of tunable dichroism measurements due to a directly applied gate bias with electrical contact made to the BP in a standard field-effect transistor (FET) geometry. Here, we observe tunability dominated by carrier concentration effects. At the band gap energy of approximately 0.53 eV, a simple decrease in absorptance is observed at negative and large positive biases, consistent with an ambipolar BM shift. Unlike the results of applying field while the BP floats, no tunability of the forbidden transition at 0.75 eV is observed; this is explained in part due to the screening of the electric field due to the carrier concentration tunability. We additionally may consider the possibility that this optical transition is disallowed by Pauli-blocking effects, negating the symmetry-breaking effect of the directly applied field. As in the case for the floating BP measurement, no tunability is observed along the zigzag axis.

### 3.2.2 8.5 nm Flake

The anisotropic electro-optical effects described above change character rapidly as the BP thickness – and hence band gap and band structure – is varied. Figure 3 presents analogous results on a flake of 8.5 nm thickness, determined by AFM (see Supporting Information, Fig. S1), for which an optical image is presented in Fig. 3a. Due to the increased thickness, the energy separation between subbands is smaller, resulting in a narrower free-spectral range between absorptance features measured in the zero-bias spectrum, presented in Fig. 3b and for which corresponding calculated optical constants are presented in Fig. 3c. Results for tunability by an external field with the BP left floating are presented in Fig. 3d. As in the thin flake, substantial tuning of the absorptance at each intersubband transition is observed due to the quantum-confined Stark effect (QCSE) red-shifting the energy of the subbands. Due to the large Stark coefficient in BP – which increases with thickness in the few-layer limit – absorption is nearly 100% suppressed, resulting in an approximately isotropic optical response from

the material.[78, 98] Unlike the previous sample, tuning of forbidden transitions is not apparent; all features correspond to transitions measured in the 0 V normalization scheme as well as the calculated optical constants for a thickness of 8.5 nm. As before, no tuning is seen along the zigzag axis, as shown in Figure S2, Supporting Information. In Fig. 3e, the tunability for directly gated, contacted BP is shown. The observed tuning – a reduction in extinction centered at each of the calculated intersubband transition energies – is relatively weak and does not persist to high photon energies. This suggests that the dominant tunability mechanism is the ambipolar BM shift, rather than the QCSE. Additional measurements at lower energies are presented in Figure S3, Supporting Information.

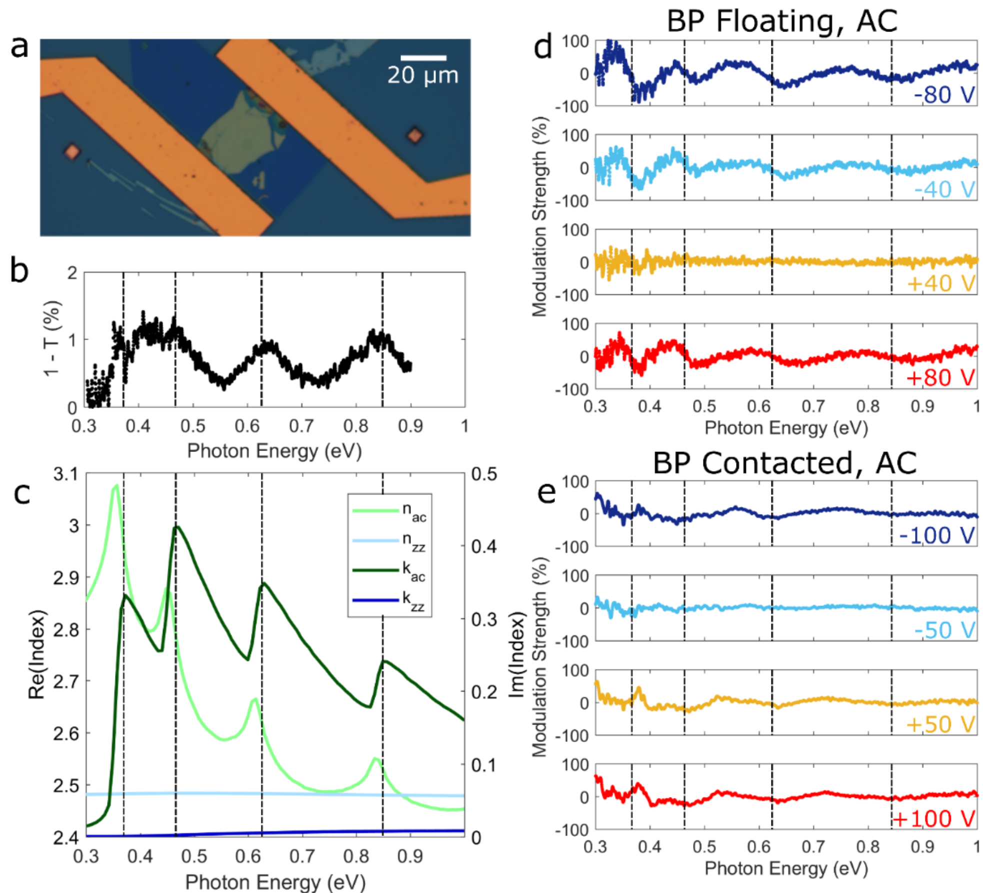


**Figure 3.3.** Variation of Tunability with BP Thickness. (a) Optical image of fabricated 8.5 nm sample. (b) Zero-bias extinction of 8.5 nm flake, polarized along AC axis. (c) Calculated index of refraction for 8.5 nm thick BP. (d) Tuning of BP oscillator strength with field applied to floating device, for light polarized along the AC axis. (e) Tuning of

BP oscillator strength with gating of contacted device, for light polarized along the AC axis.

### 3.2.3 Visible Frequency Modulation

In Figure 4 we present results of gate-tunable dichroism at visible frequencies in a 20 nm thick flake, comparable to those considered for infrared tunability. A new device geometry is used to enable transmission of visible light, shown schematically in Fig. 4a and in an optical image in Fig. 4b. In this configuration, a $SrTiO_3$ substrate is utilized to allow transmission-mode measurements at visible wavelengths. A symmetric gating scheme is devised based on semi-transparent top and back gate electrodes of 5 nm Ni, as described in the Methods section. Only an applied field, floating BP measurement is utilized, as band-filling effects should be negligible at this energy range. In Fig. 4c, we present tunability results from 1.3 to 2 eV. Due to the QCSE, tunability is observed up to 1.8 eV, corresponding to red light. Thus we demonstrate that electro-optic tuning of linear dichroism is possible across an extraordinarily wide range of wavelengths in a single material system, enabling multifunctional photonic devices with broadband operation.

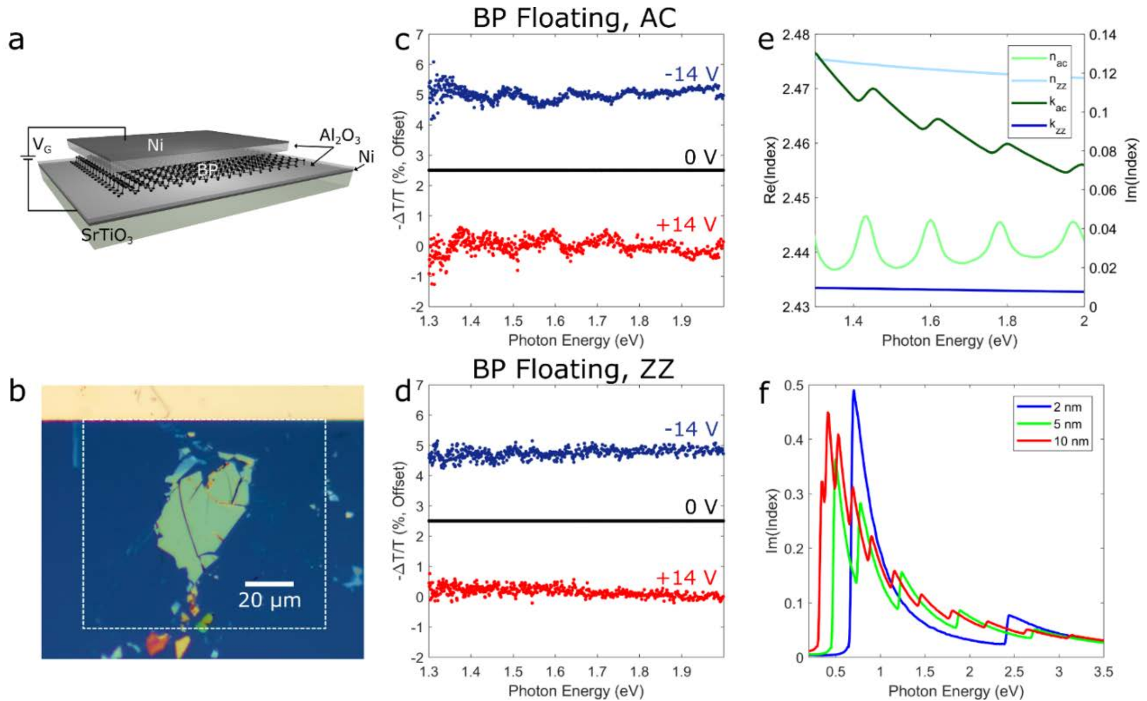


**Figure 3.4.** Tunability in the Visible. (a) Schematic figure of visible tuning device. Few-layer BP is mechanically exfoliated on 45 nm $Al_2O_3$/5 nm Ni on $SrTiO_3$ and then coated with 45 nm $Al_2O_3$. A 5 nm thick semitransparent Ni top contact is used. (b) Optical image of fabricated sample with 20 nm thick BP. Dashed white line indicates the boundary of the top Ni contact. (c) Tuning of extinction with field applied to floating device, for light polarized along the AC axis. (d) Corresponding tuning for light polarized along the ZZ axis. (e) Calculated index of refraction for 20 nm thick BP for the measured energies. (f) Calculated imaginary index of refraction of several thicknesses of BP from the infrared to visible.

The decay of BP intersubband oscillator strength at higher photon energies provides a spectral cutoff for QCSE-based tunability, but for 5 nm BP or thinner this oscillator strength is strong through the entire visible regime, as illustrated in Fig. 4f. We thus suggest that in very thin BP, strong tuning of absorption and dichroism is possible to even higher energies. By selecting a flake of 2 nm, for example, tunable linear dichroism is possible up to 3 eV from the band gap energy of 0.75 eV. A higher density of features, beginning at lower energies, may be introduced by utilizing a thicker flake, with slightly decreased tuning strength, as seen for 5 and 10 nm thickness flakes. We also note that by substituting graphene top and bottom contacts or utilizing nanophotonic techniques to focus light in the BP, higher absolute tuning strength could be easily realized.

This phenomenon is in stark contrast to the gate-tunability of the optical response of other 2D materials, where substantial tunability is typically constrained to the narrowband energy of the primary exciton, as in $MoS_2$ and $WS_2$.[71, 99] In another van der Waals materials system, monolayer graphene, tunability is accessible over a broader wavelength range due to the Pauli-blocking of optical transitions at $2E_F$; however, this is limited to the range over which electrostatic gating is effective, typically between $E_F \sim 0$ to $E_F \sim 0.5$ eV.[11, 72] Moreover, these materials are not dichroic or birefringent in-plane, and so BP offers a novel phenomenon that can be taken advantage of to realize previously challenging or impossible photonic devices. The same restriction is true of bulk tunable materials such as quantum wells, transparent conducting oxides, and transition metal nitrides.

### 3.3 Conclusions

In summary, we have demonstrated broadly tunable linear dichroism in few-layer black phosphorus. We can explain this tunability as arising from a combination of quantum-confined Stark effects, ambipolar Burstein-Moss effects, and the allowing of forbidden optical transitions by the symmetry-breaking effects of the applied electric field. We identify the different physical mechanisms governing this tunability by comparing the tunability response from a dual gate wherein the BP is left floating to a single gate directly applied to the BP, leading to tuning of carrier concentration. By varying the thickness, and therefore band structure of the BP, we see that it is possible to control the spectroscopic tunability as well as the dominant physical mechanisms of tunability. We suggest that this phenomenon is a promising platform for controlling the in-plane propagation of surface or waveguide modes, as well as for polarization-switching, reconfigurable far-field metasurfaces. These applications are particularly promising in light of our observation that BP absorption can be modulated from anisotropic to nearly isotropic in-plane. Because van der Waals materials can be easily integrated into photonic devices, this promises to introduce new functionalities that cannot be realized by conventional electro-optic materials.

# Chapter 4

# Gate-Variable Inter and Intraband Optical Transitions in a Bismuth Antimony Telluride Topological Insulator

Here, we report mid-infrared spectroscopy measurements of ultrathin, electrostatically gated $(Bi_{1-x}Sb_x)_2Te_3$ topological insulator films, in which we observe several percent modulation of transmittance and reflectance as gating shifts the Fermi level.[100] Infrared transmittance measurements of gated films were enabled by use of an epitaxial lift-off method for large-area transfer of topological insulator films from infrared-absorbing $SrTiO_3$ growth substrates to thermal oxidized silicon substrates. We combine these optical experiments with transport measurements and angle-resolved photoemission spectroscopy to identify the observed spectral modulation as a gate-driven transfer of spectral weight between both bulk and 2D topological surface channels and interband and intraband channels. We develop a model for the complex permittivity of gated $(Bi_{1-x}Sb_x)_2Te_3$, and find a good match to our experimental data. These results open the path for layered topological insulator materials as a new candidate for tunable, ultrathin infrared optics and highlight the possibility of switching topological optoelectronic phenomena between bulk and spin-polarized surface regimes.

## 4.1 Introduction

Topological insulators – narrow band-gap semiconductors that exhibit both an insulating bulk and metallic Dirac surface states – have been found experimentally in the past several years to display a remarkable range of new electronic phenomena.[13, 14, 17, 101] In addition, these Dirac surface states have been predicted to host unique and technologically compelling optical and optoelectronic behavior. Some of these effects have been experimentally demonstrated – giant magneto-optical effects, helicity-dependent photocurrents and more – but many others, including gapless infrared photodetection, gate-tunable, long-lived Dirac plasmons and hybrid spin-plasmon modes, remain elusive.[18-22, 56, 102-107]

One of the most fascinating features of topological insulator systems is the coexistence and interplay of massless Dirac electrons and massive bulk carriers. While systems like the bismuth telluride family of materials are strong topological insulators, they are also structurally two-dimensional, layered Van der Waals semiconductors.[15, 16] For

technologies like tunable optics, for which the graphene Dirac system is promising, excitations of both Dirac electrons and these low effective mass bulk carriers are equally compelling.[59, 108-110] The low density of states of both of these classes of carriers and availability of ultrathin, gate-tunable films by Van der Waals epitaxy indicate the possibility of highly tunable infrared absorption.[64, 111] Furthermore, by tuning the Fermi level of these materials it may be possible to switch dynamically between optoelectronic regimes dominated by spin-polarized topological surface physics and by bulk semiconductor physics.

In this paper, we report a measurement of the infrared reflectance and transmittance of ultrathin $(Bi_{1-x}Sb_x)_2Te_3$ (x = 0.94) topological insulator (TI) films while applying a gate voltage to modulate the Fermi level. To allow gated transmittance measurements, we developed an epitaxial lift-off method for large-area transfer of TI films from the infrared-absorbing $SrTiO_3$ growth substrates to thermal oxidized silicon substrates.[112, 113] We combine these optical experiments with gated transport measurements and angle-resolved photoemission spectroscopy to identify the mechanism of the observed spectral modulation. This behavior consists of a gate-driven transfer of spectral weight between both bulk and 2D topological surface channels and interband and intraband channels. We propose that the physical bases for these phenomena are Pauli-blocking of bulk interband transitions, for higher photon energies, and modulation of the plasma edge with varying topological surface and bulk carrier densities, for lower photon energies. We develop a model for the complex permittivity of gated $(Bi_{1-x}Sb_x)_2Te_3$, and find a good match to our experimental data.

## 4.2 Experimental Measurements of the Bismuth Antimony Telluride Optical Response with Doping by an Electrostatic Gate

Our experimental optical setup and device structure are shown in Figure 4.1. The topological insulator film sits atop a thermally oxidized silicon substrate, allowing control of its Fermi level by applying a voltage between electrodes on the film and the doped silicon to accumulate or deplete carriers by the field effect.[114] As depicted in Figure 4.1,

the topological surface state is thought to occupy a 1 – 2 nm region at the top and bottom interfaces of the $(Bi_{1-x}Sb_x)_2Te_3$ film.[115] An optical microscope image and AFM cross-cut are shown for a $(Bi_{1-x}Sb_x)_2Te_3$ film transferred from its growth substrate to thermally oxidized silicon and patterned into an electrically isolated device.

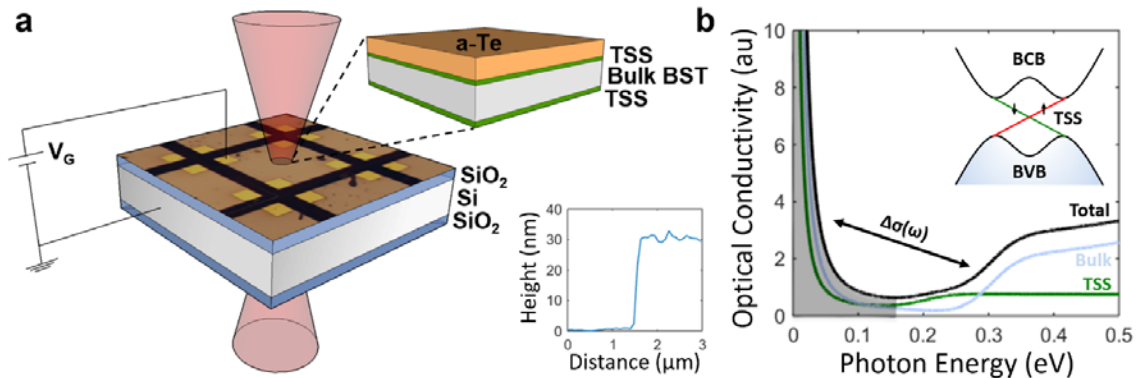


**Figure 4.1**: Schematic of experiment. **a)** Schematic of setup. The sample structure consists of a 10 nm a-Te layer atop a 20 nm $(Bi_{1-x}Sb_x)_2Te_3$ (BST) film on 285 nm thermal oxide on silicon. The metallic topological surface states in the BST penetrate 1-2 nm into the insulating bulk. The transmittance and reflectance of this stack are probed by an FTIR spectrometer coupled to an infrared microscope as the gate voltage is modulated. Inset: AFM cross-cut of transferred film, showing 30 nm total height of a-Te and BST. **b)** Schematic of observed behavior. The optical response of the BST consists of contributions from bulk and topological surface carriers.[116] With changing gate voltage, spectral weight is transferred between both bulk (blue) and topological surface (green) channels and between interband (unshaded region) and intraband (shaded region) channels, as indicated by the arrow. Inset: Schematic band structure of BST, with bulk valence and conduction bands, topological surface states and 0.3 eV band gap indicated.

### 4.2.1 Epitaxial Lift-Off of Bismuth Antimony Telluride

Bismuth antimony telluride is a state-of-the-art topological insulator alloy, and thus far is available only via molecular beam epitaxy on a small number of growth substrates. None of these substrates are simultaneously suitable for both field-effect gating and infrared characterization, so to enable these experiments it was necessary to transfer the epitaxial films to a new substrate. We developed a method for wet transfer of bismuth antimony telluride from strontium titanate to thermal oxide on silicon, adapted from work on other chalcogenides in Reference [112]. This process and a transferred film are shown in Figure

4.2. After spin-coating PMMA (950 A8) onto the surface of the films and baking them on a hot-plate at 170 C for 2 minutes, the chips are placed into a bath of buffered hydrofluoric acid. The film begins peeling off the substrate after 2-3 hours, at which point the chip is placed into a series of DI water baths. The chip is held at the surface of the water, and surface tension is used to complete peeling of the film. The film floats on the surface of the water, and is lifted out with a thermal oxide on silicon chip. This chip is dried overnight, and the PMMA is removed with acetone.

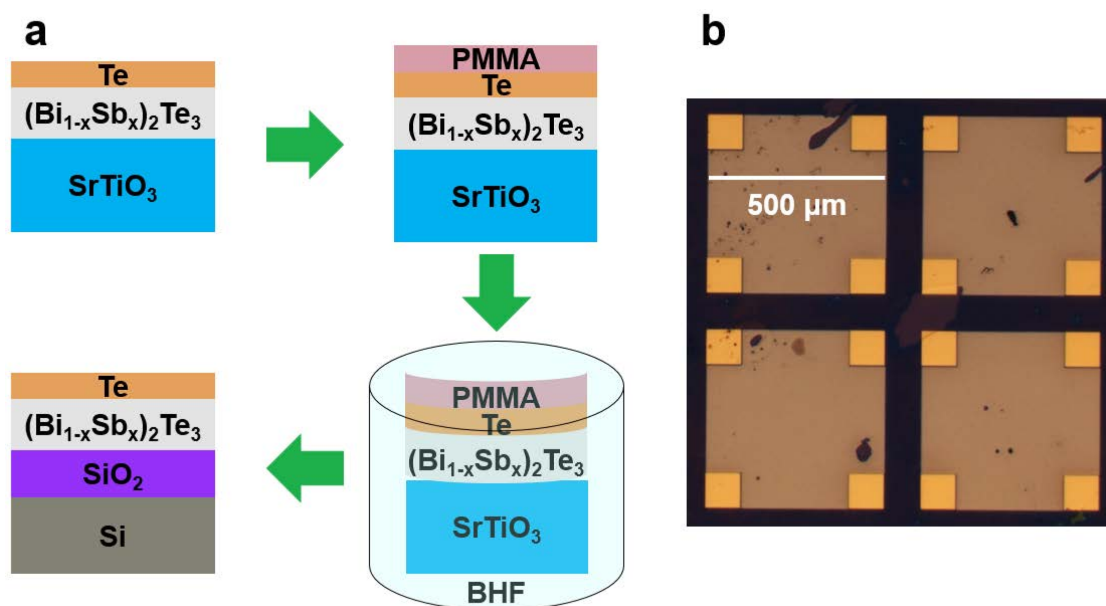


**Figure 4.2**: Transfer method and result. **a)** Outline of transfer process. PMMA is spin-coated onto $(Bi_{1-x}Sb_x)_2Te_3$ film on its STO growth substrate. The sample is then submerged into buffered HF until the PMMA / Te / $(Bi_{1-x}Sb_x)_2Te_3$ stack peels from the STO. The stack is scooped out of water with a $SiO_2$ / Si chip, dried, and treated with acetone to remove the PMMA. **b)** Optical microscope image of devices fabricated on a film transferred to $SiO_2$ / Si.

### 4.2.2 Infrared Optical Response

The primary result of this work is the observation of gate-control of inter and intra-band optical transitions in transmittance and reflectance, presented in Figure 4.3. Infrared transmittance and reflectance are probed using an infrared microscope coupled to an FTIR spectrometer, while the gate bias is varied. Modulation of transmittance and

reflectance of several percent is observed, with respect to their values at zero-bias applied to the silicon gate. In transmittance, two major features are seen. At lower photon energies, transmittance is increased as the Fermi level is increased. At higher photon energies, transmittance is decreased as the Fermi level is increased. Between these features – labelled A and B, respectively, in Figure 4.3b – is an isosbestic point that sees no modulation, suggesting a cross-over between two competing effects.

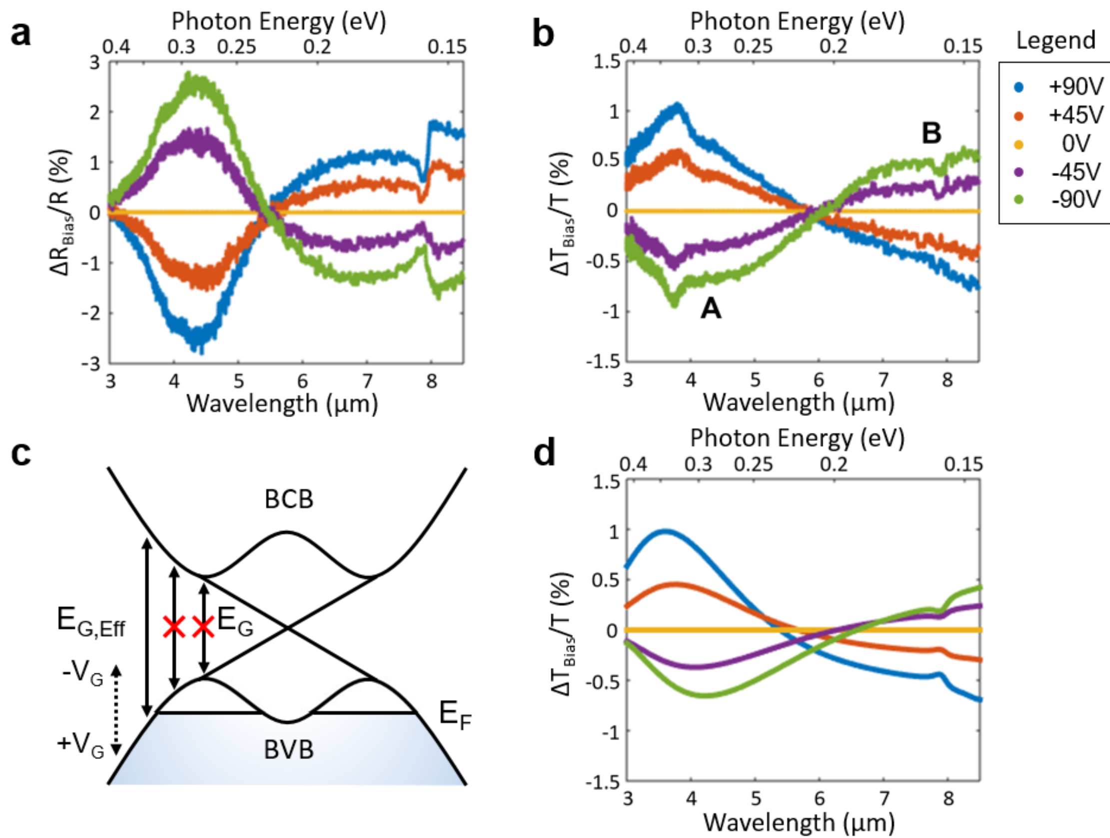


**Figure 4.3**: Gate-variable FTIR reflectance and transmittance. **a)** Change in reflectance with electrostatic gate bias at T = 78 K, normalized to the zero-bias case. **b)** Change in transmittance with gate bias at T = 78 K, normalized to the zero-bias case. Similar behavior is observed at room T, but with lower modulation strength. **c)** Schematic of the Burstein-Moss effect. As $E_F$ decreases into the BVB, lower energy bulk interband transitions are forbidden. The bulk band gap energy is approx. 300 meV / 4.1 μm. **d)** Modelled transmittance based on a combined model of gate-variable Pauli-blocking / Burstein-Moss shifting of bulk interband transitions, for higher photon energies, and modulation of the plasma edge with varying topological surface and bulk carrier densities, for lower photon energies. As a simple model of the Burstein-Moss shift, band edge optical constants are shifted in energy-space. Varying surface and bulk free carrier contributions to the dielectric function are modelled by the Kubo and Drude models, respectively, and a simple capacitor

model of carrier density modulation. From Hall, transport and ARPES results, the zero-bias carrier density is estimated to be 30% topological surface carriers and 70% bulk carriers.

### 4.2.3 Transport Characterization

To locate the Fermi level in our films, we measured the sheet-resistance as functions of gate voltage and temperature, as presented in Figure 4.4. With negative gate bias, sheet resistance is seen to increase as p-type carriers are depleted by the field effect and the Fermi level of our film is increased. At large negative bias, the resistance appears to approach a peak that, while not visible in our range of gate voltages, we speculate may be the Dirac point. Likewise, with positive bias, sheet resistance is seen to decrease as p-type carriers are accumulated and the Fermi level is decreased. In measurements of sheet resistance versus temperature, a transition from metallic to insulating character is seen as the gate bias passes -40 V – indicating that the Fermi level has crossed the bulk valence band edge.[117] Angle-resolved photoemission spectroscopy (Figure 4.4c) is used to map the band structure of $(Bi_{1-x}Sb_x)_2Te_3$ in this region. We note that these photoemission spectroscopy results only approximate the band structure in our transferred films, which will vary due to modified doping. The total carrier density in the film at zero bias, $n_{2D} = 2.5 \cdot 10^{13}$ cm$^{-2}$, is obtained from Hall measurements.

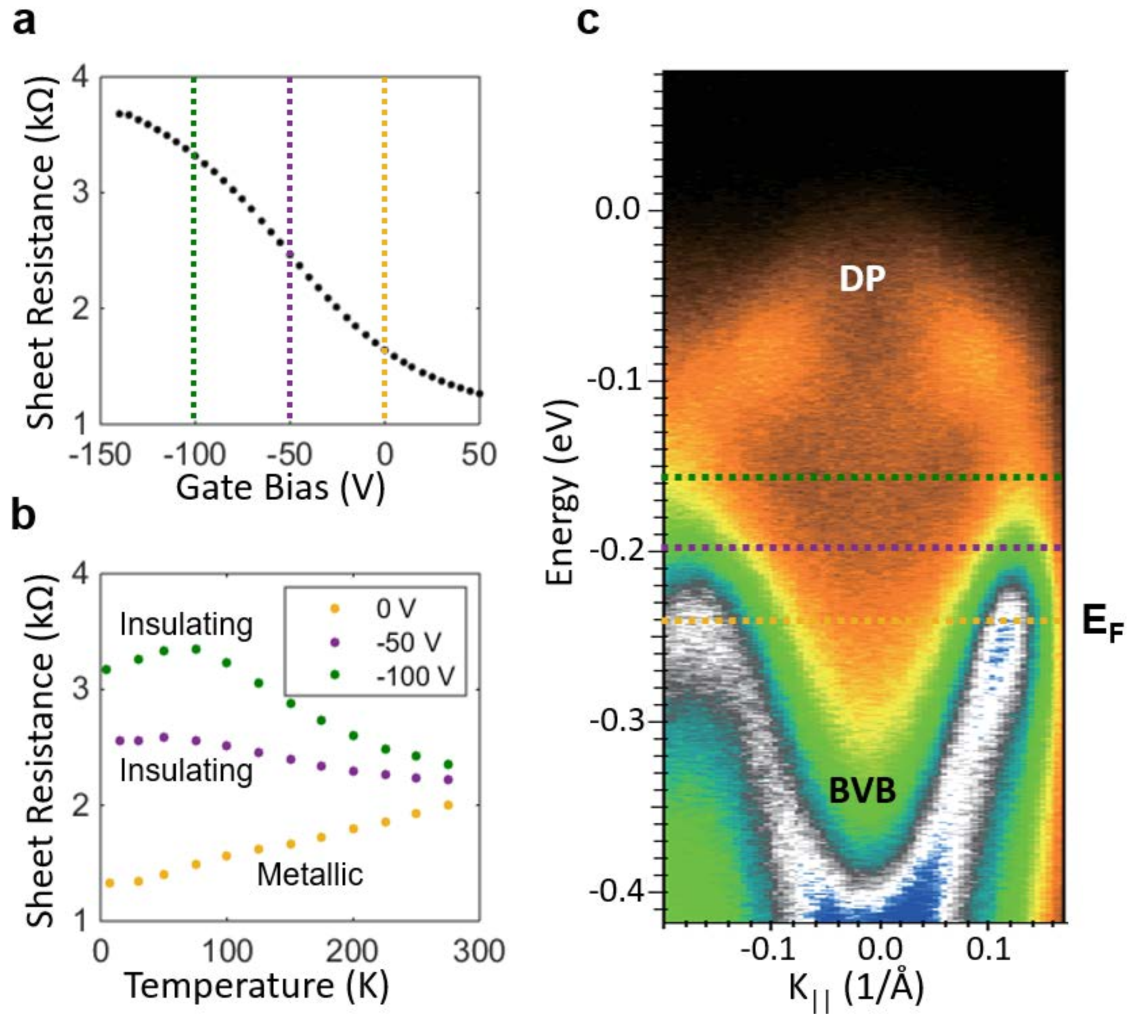


**Figure 4.4**: Electrical characterization and gate-driven metal-insulator transition. **a)** Sheet resistance ($R_{sh}$) of film versus bias applied over $SiO_2$ gate dielectric at T = 4.2 K. $R_{sh}$ increases with decreasing $V_g$ / increasing $E_F$, indicating initial hole doping. The $R_{sh}$ value appears to approach a maximum at large negative bias, which, while not observed here, we speculate to be the Dirac point. Further electrostatic doping results in electrical breakdown. **b)** $R_{sh}$ versus T at three $V_g$ levels indicates a transition from metallic behavior, where R increases with T, to insulating behavior, where R decreases with T. At this transition voltage, approximately -40 V, the Fermi level crosses the bulk valence band edge. **c)** Schematic illustrating $E_F$ (color-coded dashed lines) crossing the bulk valence band (BVB) edge at the metal-insulator transition voltage, overlaid on ARPES results for a similar $(Bi_{1-x}Sb_x)_2Te_3$ film, including the main features of the band structure. Inside the bulk gap are the two spin-polarized Dirac bands.

From transport measurements, we conclude that unbiased $(Bi_{1-x}Sb_x)_2Te_3$ films are hole-doped, with a Fermi level position slightly below the bulk valence band edge. The modulation of sheet resistance seen with gating indicates that the Fermi level of the entire film is modified by the gate. However, band bending is expected and the effect of gating is thus stronger near the oxide interface, as shown in Figure 4.6.[56, 111] We estimate the screening length in the $(Bi_{1-x}Sb_x)_2Te_3$ film to be of order 10 nm, as is discussed in the Supporting Information. The observed modulation further suggests that electrostatic gating is forcing the film between regimes where topological surface carriers and bulk carriers are expected to dominate the conductivity, respectively. The $R_{sh}$ on-off ratio is much lower than that seen in films of other layered materials with a similar thickness and band gap, such as black phosphorus, consistent with the presence of a conductive topological surface state that shorts the insulating ‘off’ state of the field effect device.[30]

Given the identified Fermi level position of the film, we suggest that feature A in the optical response at higher photon energies is driven by gate-modulation of interband transitions via population of bulk valence band states with holes. As shown in Figure 4.3c, a doped semiconductor has a characteristic effective bandgap defined – for hole-doped samples – by the distance from the Fermi level to the conduction band. In the $(Bi_{1-x}Sb_x)_2Te_3$ system investigated here, this Fermi level shifts with $V_g$, altering the allowed and forbidden optical transitions and hence its band edge optical constants. Similar behavior is seen for electrostatic doping in graphene, and for chemical doping in narrow-band-gap semiconductor materials, in which it is known as the Burstein-Moss effect.[12, 64, 118, 119] This behavior is seen only in thin films of materials with a low density of states, and indicates possible technological applications for narrow-gap TI materials as optoelectronic modulators. The observed modulation persists at room temperature, albeit with a lower strength. At a temperature of 5 K, as discussed in Section 4.2.4, the band-edge modulation is stronger and sharper – indicative of a narrower Fermi distribution – and an additional feature appears. The resulting change in the optical band gap can be approximated as follows, where $H(E_{BVB} - E_F, T)$ is a Heaviside step-function with a

temperature-dependent broadening that accounts for the width of the Fermi-Dirac distribution.[120]

$$\Delta E_G = 2\Delta(E_{BVB} - E_F)H(E_{BVB} - E_F,\, T) \qquad (4.1)$$

We propose that feature B in the optical response at lower photon energies is characterized by a change in the intraband absorption associated with both topological surface states and bulk states. While depressing the Fermi level into the bulk valence band will decrease the band-edge interband transition rate – increasing transmittance near the band edge – it simultaneously transfers spectral weight to intraband channels, increasing absorption and decreasing transmittance at lower energies. We suggest that the physical mechanism of this change in intraband absorption is the modulation of carrier density in the film – by as much as 27 percent – via electrostatics. This behavior indicates the possibility of extending the tunable, mid-infrared Dirac plasmons seen in graphene to spin-polarized topological insulator materials.[11, 21, 72]

This conjecture is supported by our transport data, which indicates that the Fermi level is shifting back and forth across the bulk valence band edge, but transmittance can also be modeled directly using measured values and one free fitting parameter. A simple picture of the modulated bulk interband absorption is provided by experimental measurements of the band edge dielectric function, which was determined from infrared ellipsometry measurements of an as-grown $(Bi_{1-x}Sb_x)_2Te_3$ film on sapphire. The change in the band edge dielectric function energy as a function of gate voltage, is modeled by shifting the zero-bias dielectric function by an energy $\Delta E_S$, proportional to the corresponding voltage, such that the dielectric function as a function of gate voltage can be described by a single free parameter.

#### 4.2.4 5 K Measurements

Lastly, we note that interband transitions between topological surface state bands should fall within the energy range of our measurements. Gate-variable FTIR transmittance is

also measured at 5 K, in order to understand the low temperature infrared response of the $(Bi_{1-x}Sb_x)_2Te_3$ film and look for TSS to TSS interband transitions. These measurements are performed in a modified Oxford cryostat using a Bruker Lumos infrared microscope and spectrometer, in the Basov Lab facilities at UCSD. The behavior seen – shown in Figure 4.5 – is consistent with that seen at 78 K, with a smaller Fermi-Dirac distribution width. An additional kink feature is seen near six microns, but no clear evidence of TSS to TSS interband transitions – which should show a universal optical conductivity of $\pi e^2/8h$ above $2E_F$ – is seen.[116] The presence of accumulating ice dampens the modulation around a narrow feature at three microns.[121]

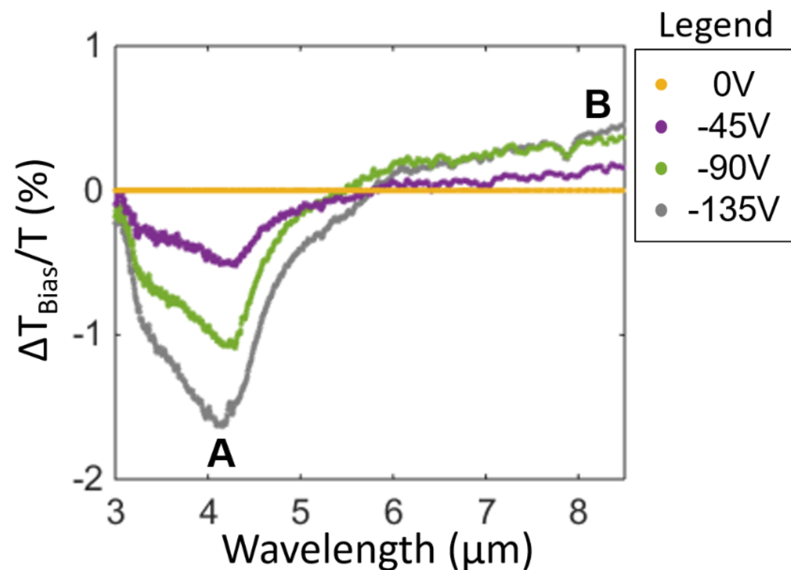


**Figure 4.5**: Gate-variable FTIR transmittance at T = 5 K. Transmittance is shown normalized to zero bias case, as the Fermi level is pushed into the bulk band gap and towards the Dirac point. Similar behavior is seen as in T = 78 K, with two main differences. The band-edge Pauli-blocking effect is sharper and more pronounced, likely due to narrowing of the Fermi-Dirac distribution of carrier energies. There also appears a kink feature in transmittance near 6 microns. This feature may be related, but no clear evidence of TSS to TSS interband transitions is observed.

### 4.3 Dielectric Function and Transfer Matrix Model

To model the optical response at small negative Fermi level positions, the topological surface state and bulk carrier densities are first parameterized as a function of gate

voltage. From our fit of the absorption-edge energy shifts, a gate voltage of $V_g$ = +/- 45V corresponds to a shift of the Fermi level of approximately 28 meV. The observed metal-insulator transition occurs at $V_g \approx 40$V, so the Fermi level at zero bias must be at approximately (28 meV · 40 V / 45V) = 25 meV below the bulk valence band edge. The bulk valence band is observed to be 150 meV below the Dirac point in angle-resolved photoemission measurements, indicating a Fermi level of $E_F$ = -175 meV relative to the Dirac point.[16] The topological surface state carrier density can be calculated from this Fermi level by assuming the electronic structure is characterized by the well-known topological surface state dispersion relation.[16, 122] We find that $n_{TSS} = k_F^2/4\pi = 4 \cdot 10^{12}$ cm$^{-2}$ for each surface, where $k_F = E_F/\hbar v_F$. Including both surfaces, our topological surface state density / bulk carrier density ratio is found to be approximately $n_{2D,TSS}/n_{2D} = 30\%$. As our films are deeply subwavelength in thickness, we model the $(Bi_{1-x}Sb_x)_2Te_3$ film as having a single effective dielectric function that includes contributions from both of these types of carriers, as well as interband absorption, as discussed above. The intraband dielectric functions for the topological surface state and bulk free carriers were treated using Kubo and Drude models, respectively.[123, 124]

$$\varepsilon(\omega) = \varepsilon_{\text{interband}}(\omega, E_F, T) + \varepsilon_{\text{intraband, TSS}}(\omega, n_{\text{2D,TSS}}) + \varepsilon_{\text{intraband, bulk}}(\omega, n_{\text{2D,bulk}})$$

$$= \varepsilon_{\text{interband}}(\omega, E_F, T) - \frac{e^2 v_F}{d\hbar\omega\left(\omega + \frac{i}{\tau}\right)}\left(\frac{n_{\text{2D,TSS}}}{2\pi}\right)^{1/2} - \frac{e^2 n_{\text{2D,bulk}}}{dm\omega\left(\omega + \frac{i}{\tau}\right)} \qquad (4.2)$$

This dielectric function model is combined with a simple capacitor model that defines the change in carrier concentration with gate voltage – up to 27 percent at 90 V. The charge on each plate is given by $Q = V_g C$, where the capacitance C is calculated to be 12 nF/cm$^2$ for the 285 nm $SiO_2$ using a standard parallel plate geometry.[125] Combining these elements, we use the transfer matrix method to calculate transmittance (Figure 4.3d) through the $(Bi_{1-x}Sb_x)_2Te_3$ film and substrate stack.[126] The modeled values for $\Delta T/T$ – based on experimental parameters and a single fitting parameter – yield a close match to our experimental results.

We note that band bending, as described in Figure 4.6, adds an additional degree of complexity to this system, and that as the screening length in the films is similar to their thickness, transport and optical measurements will not respond identically to gating.[56, 111, 127] Due to these differences and any variation in band structure between our samples and those investigated by Zhang, et al., we present the above analysis as an approximate model intended to demonstrate qualitative agreement between our experimental results and our description of the physical basis.[16] We further note two smaller features seen in FTIR spectra. In Figure 4.3a,b a small dip in transmittance and reflectance modulation is seen near 8 microns, which we attribute to absorption in the silicon oxide due to the presence of a phonon line. In Figure 4.3b, a small peak in transmittance modulation is seen near 3.8 microns. We speculate that this peak may be due to a defect state or subband, and add that it persists in room temperature measurements and is thus unlikely to be excitonic in nature.[103, 128-130]

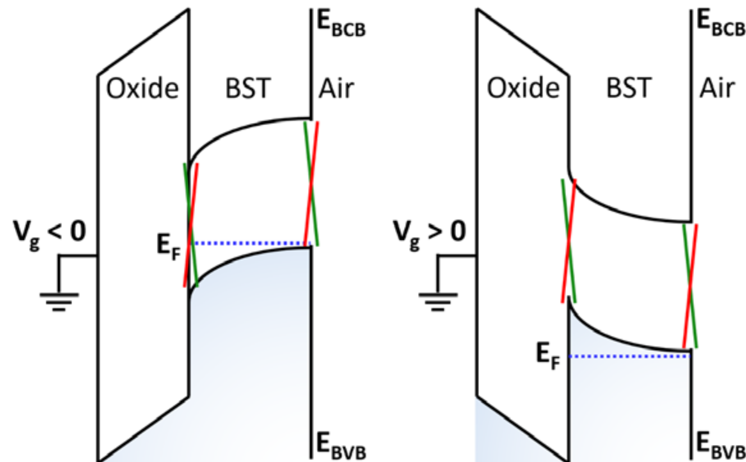


**Figure 4.6**: Schematic of energy bands across sample structure. Energy bands are shown for the silicon oxide, BST surfaces (green and red, at interfaces), BST bulk, and air. For negative bias, additional holes are accumulated in the BST layer. For positive bias, holes are depleted. The screening length is of order the width of the BST layer. As a result, the two topological surfaces likely experience different doping. Due to the much lower doping in the a-Te, band bending at the BST / a-Te interface occurs mostly in the a-Te and so is not shown here.

## 4.4 Conclusions

In conclusion, we have experimentally investigated the mid-infrared optical response of $(Bi_{1-x}Sb_x)_2Te_3$ films as the Fermi level position is varied by electrostatic gating. This response is characterized by a gate-driven transfer of spectral weight between both bulk and 2D topological surface channels and interband and intraband channels. We associate the higher photon energy behavior with Pauli-blocking of bulk interband optical transitions, and the lower energy behavior with modulation of the plasma edge with varying topological surface and bulk carrier densities. These results present layered topological insulator materials as a new candidate material for ultrathin, tunable infrared photonics and illustrate the possibilities for switching topological optoelectronic phenomena – tunable, mid-infrared Dirac plasmons, hybrid spin-plasmons and more – between bulk and spin-polarized surface regimes.

# Chapter 5

# Phase, Amplitude and Polarization Modulation in Few-Layer Black Phosphorus Microcavities

Here, we present theoretical results indicating that a double distributed Bragg reflector microcavity loaded with black phosphorus acts as an effective phase, amplitude, and polarization modulation device. We observe 246 degrees of phase modulation with a reflectance intensity maintained above 75 percent in a structure operating at 2397 nm, and amplitude modulation with greater than 98 percent modulation depth and an off-state with less than 0.1% reflectance in another structure operating at 2054 nm. Due to the in-plane structural and optoelectronic anisotropy of black phosphorus, these devices additionally function as an electrically-tunable waveplate and linear polarizer, respectively. The working wavelength of these devices may be tuned by to 1550 nm or other important frequency bands using a different thickness of black phosphorus. These promising results suggest both that experimental confirmation of these findings should be urgently pursued, and that black phosphorus has a bright future in active photonics.

## 5.1 Introduction

Over the past several years, a variety of passive metasurface devices have been developed to control the amplitude, phase, and polarization of incident light.[3] A grand challenge for nanophotonics is to develop active metasurfaces that can control these variables as a function of time, allowing the truly complete control of radiation. Nanophotonic unit cells that can control the phase and amplitude of incident light with low loss are critical building blocks of such devices. With these building blocks, active metasurfaces can be designed for complex wavefront engineering, including the directional steering of reflected or transmitted light, as depicted in the example schematic in Figure 5.1.[89] When reconfigured electrically, such metasurface devices can operate at gigahertz speeds, a serious advantage for many applications, including solid-state metasurface lidar.

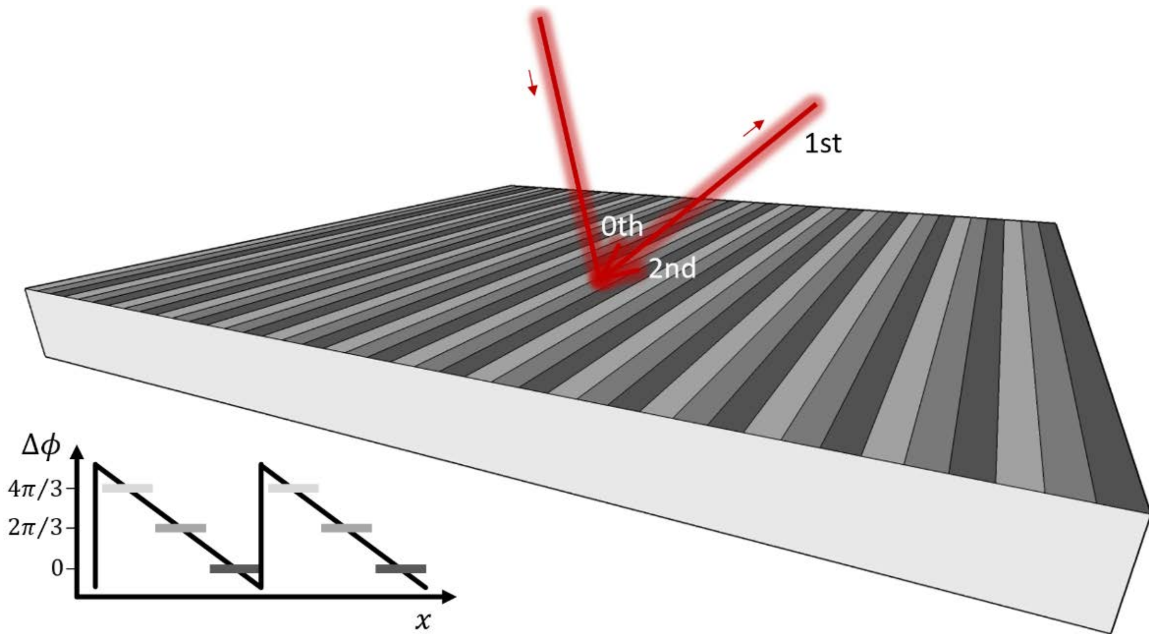


**Figure 5.1**: A schematic, 1D active metasurface designed to achieve optical beam steering. A spatial sequence of varying phase shifts upon reflection from the metasurface simulates the response of a blazed grating, as illustrated in the inset. The resulting phase surface directs the reflection of an incident laser beam into a target outgoing diffraction order – in this case, the $1^{st}$ – and angle that can be tuned by modifying its pitch. An ongoing challenge is design efficient metasurface unit cells that can provide variable, electrically-tunable phase shifts upon reflectance with low overall loss.

This schematic depicts an electrically controlled reflectarray metasurface that steers light into a target diffraction order defined by a spatial sequence of phase shifts that simulates a blazed grating. The angle at which reflected light is steered into this diffraction order is dictated by the grating pitch, $d$, as described by the grating equation.

$$m\lambda = d(sin\theta_i \pm \sin\theta_r) \qquad (5.1)$$

With still more complex structures and ideal phase control, arbitrary 2D holography can be performed.[131] A primary obstacle to these technologies is the design of tunable unit cells that can provide a large range of electrically-driven phase modulation while maintaining uniform, high reflectance and low loss.

The development of nanophotonic structures that simultaneously provide large reflected phase tunability with high, near-constant reflectance is a challenge, and will require innovation in both materials and nanophotonic design. One metric by which to compare possible tunable elements is the electrically-induced change in the real part of the refractive index, divided by its imaginary part. For plasmonic materials with high loss, large refractive index tunability can be achieved, but this ratio remains relatively low. The same is true of tunable excitonic features in 2D materials.[132] For this reason, tunable dielectric structures such as semiconductor quantum wells are promising. Few-layer black phosphorus, which acts as a natural, anisotropic quantum well, has been shown to exhibit strong electro-optical modulation, and so is a favorable candidate for this application.[23, 80]

### 5.2 Theory Results for Phase, Amplitude and Polarization Modulation

We design a double distributed Bragg reflector microcavity for two purposes: to enhance light-matter interactions between the incident radiation field and the black phosphorus, and to create an optical resonance that sweeps a range of reflected phase and amplitude values. To model the phase and amplitude modulation possible in this structure, transfer matrix methods in the Lumerical FDTD software package were used to calculate reflected phase and intensity as the black phosphorus refractive index is varied. The black phosphorus refractive index data for different carrier density values is taken from calculations in Reference [60]. As seen in previous work, we assume modulation of the zig-zag axis refractive index is negligible. We assume a black phosphorus thickness of 5 nm, to match those available calculated values.

For phase modulation, where simultaneous amplitude modulation is undesirable, we choose to design a cavity that is resonant below the band edge of 5 nm black phosphorus, where absorption is low but substantial refractive index changes with doping persist. The double distributed Bragg reflector structure evaluated consists of a conductive, 40 pair AlAs / $Al_{0.1}Ga_{0.9}As$ bottom reflector on a GaAs substrate, a 10 nm $Al_2O_3$ gate dielectric, a 5 nm black phosphorus layer, and a 10 pair $SiO_2$ / $SiN_x$ top reflector. All reflector layers have thicknesses of $\lambda/4n$.

The calculated phase modulation results are presented in Figure 5.2. Reflected phase is tuned across 246 degrees at approximately 2397 nm for this structure, while reflectance intensity is maintained above 75 percent. To the best of the authors' knowledge, this reflectance loss is lower than other published electrically-tunable, far-field devices with similar or higher phase modulation.[87, 89] Further, the armchair-axis reflected phase value sweeps through the zig-zag axis value near a carrier density of $1x10^{13}$ $cm^{-2}$. As a result, in addition to typical phase modulation, this device can act as an electrically tunable waveplate, converting circularly or elliptically polarized light to linearly polarized light and vice versa.

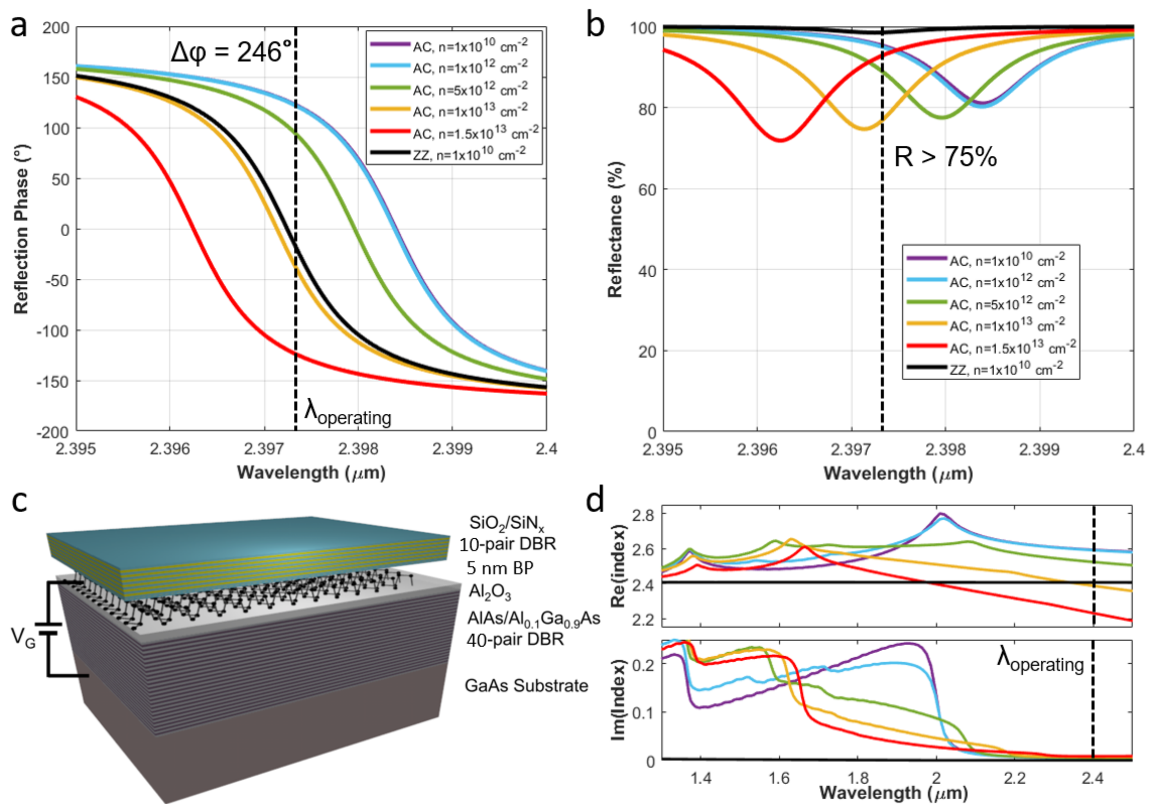


**Figure 5.2**: A design for a black phosphorus reflected phase modulator. **a)** Calculated reflected phase response for the device, for both crystal axes and a range of injected carrier densities. **b)** Calculated reflectance intensity for the device, for both crystal axes and the same range of injected carrier densities. **c)** Structure schematic. **d)** Real and complex refractive index for 5 nm black phosphorus, from theory.

As the quality factor of the microcavity is increased, which is straightforward by increasing the number of pairs in the top Bragg reflector, the reflected phase modulation increases, but the reflectance intensity minimum decreases. The tradeoff is shown in Figure 5.3, and allows the device performance to be optimized.

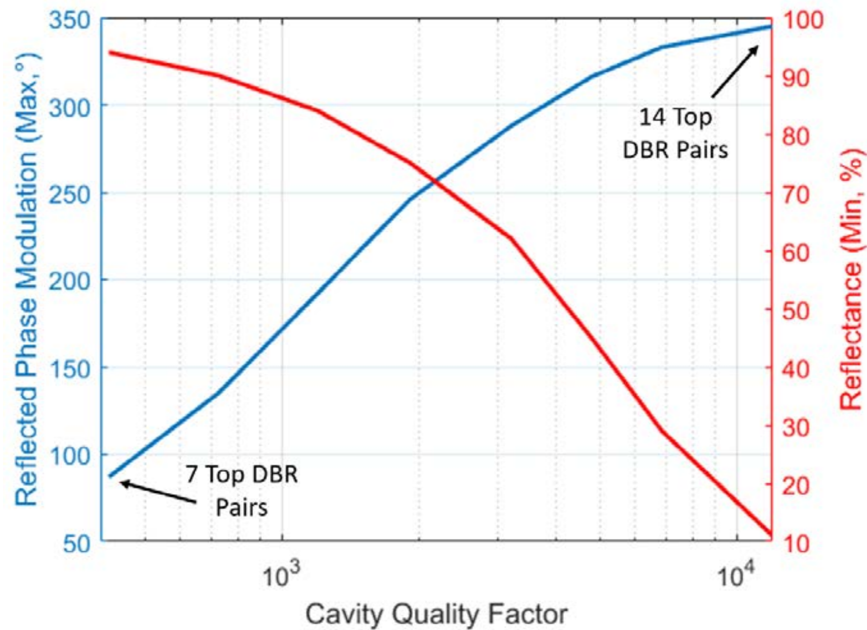


**Figure 5.3**: A design for a black phosphorus reflected phase modulator. **a)** Calculated reflected phase response for the device, for both crystal axes and a range of injected carrier densities. **b)** Calculated reflectance intensity for the device, for both crystal axes and the same range of injected carrier densities. **c)** Structure schematic. **d)** Real and complex refractive index for 5 nm black phosphorus, from theory.

A nearly identical structure is used to achieve amplitude modulation. To increase absorption and enhance the modulation depth, the Bragg reflector layer thicknesses are adjusted to move the operating wavelength closer to the black phosphorus band edge, at approximately 2054 nm. A 12 pair top Bragg reflector is used to further increase the modulation depth. This device is presented in Figure 5.4. More than 98% modulation depth is observed, with an off-state reflectance below 0.1%. Minimal reflected phase modulation is observed, except in the trivial case where the reflectance is near zero, indicating nearly pure amplitude modulation. Further, the armchair-axis reflectance intensity closely approaches that of the zig-zag axis at a carrier density of $1.5\text{x}10^{13}$ $\text{cm}^{-2}$.

As a result, in addition to typical amplitude modulation, this device functions as a tunable linear polarizer, able to convert unpolarized light to linearly polarized light.

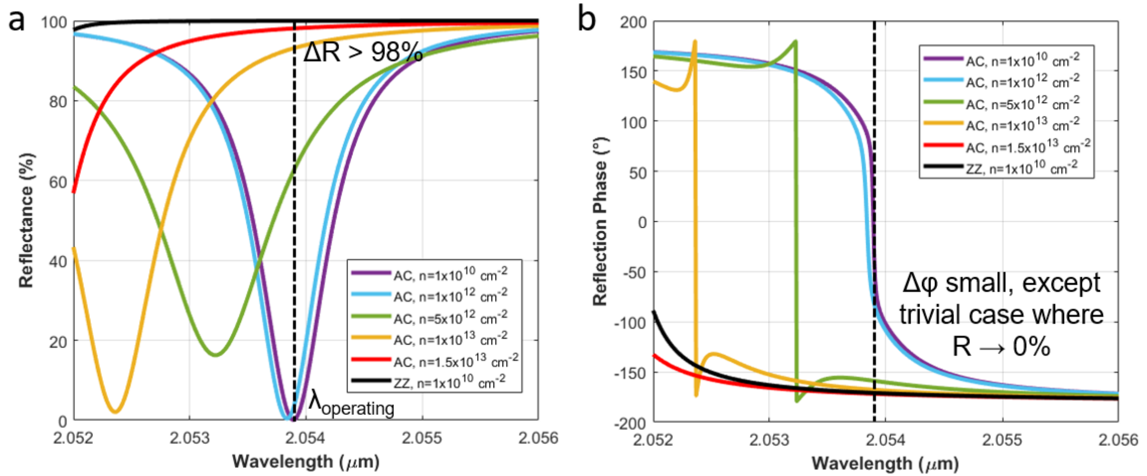


**Figure 5.4**: A design for a black phosphorus reflectance amplitude modulator. **a)** Calculated reflectance intensity response for the device, for both crystal axes and a range of injected carrier densities. **b)** Calculated reflected phase response for the device, for both crystal axes and the same range of injected carrier densities.

We note that the promising performance observed for phase and amplitude modulation in 5 nm black phosphorus at 2397 nm and 2054 nm, respectively, can in principle be tuned across the near-infrared by adjusting the thickness of the black phosphorus. While the band structure and Stark coefficient of the material change significantly with thickness, it is likely that efficient modulation can be achieved at technologically important frequency bands such as the 1550 nm C band used for telecommunications. The epitaxial growth of black phosphorus remains a challenge. However, there is hope that its integration into semiconductor device may soon be simpler and lower cost than the production of compound semiconductor quantum wells, due to the lack of lattice matching requirements, and viability of metallo-organic chemical vapor deposition. A critical next step will be to confirm these theoretical findings experimentally.

### 5.3 Conclusions

Active metasurfaces are a technologically compelling and rapidly developing research area. To enable the promising directions that researchers have envisioned for this field, ideal phase and amplitude modulation elements must be developed. Few-layer black phosphorus is an emerging van der Waals material well-suited to optoelectronic applications across the near-infrared. We demonstrate theoretical results showing 246 degrees of phase modulation with a reflectance intensity maintained above 75 percent at a wavelength of 2397 nm in a double distributed Bragg reflector microcavity loaded with black phosphorus. We further show amplitude modulation in a similar structure at 2054 nm, with greater than 98 percent modulation depth and an off-state with less than 0.1% reflectance. Due to the in-plane structural and optoelectronic anisotropy of black phosphorus, these devices additionally function as an electrically-tunable waveplate and linear polarizer, respectively. These promising results suggest both that experimental confirmation of these findings must be urgently pursued, and that black phosphorus has a bright future in optoelectronic applications.

# Chapter 6

# Ongoing and Future Work and Perspective

## 6.1 Ongoing and Future Work

The discovery and understanding of novel light-matter interactions in new materials promises to provide new mechanisms for the control of light at the nanoscale. We describe here three experiments – the first two ongoing, and the last proposed – that we believe represent important directions for fundamental and applied research in this area. The first is a fundamental study of the unique plasmonic properties predicted to exist in black phosphorus. The second is an experimental program designed to follow up on the theoretical results presented in Chapter 5, which suggest that few-layer black phosphorus quantum wells are an ideal component for future phase modulation, beam-steering and polarization control devices. Lastly, we describe two experiments to seek demonstration of hybrid spin-charge plasmon modes – a fundamentally new type of light-matter interaction – in bismuth antimony telluride.

### 6.1.1 Plasmons in Few-Layer Black Phosphorus

Surface plasmons polaritons, quasiparticles consisting of a photon coupled to oscillations of the free charge density, are promising for nanoscale guiding of light, strong coupling of quantum and optoelectronic systems, light-enhanced catalysis, thermal management and an expanding array of other applications.[133, 134] Surface plasmons in black phosphorus have yet to be experimentally demonstrated, with the exception of recent observations of a related surface-phonon-plasmon-polariton hybrid mode in a black phosphorus heterostructure.[135] However, these surface plasmon modes are predicted to have a number of unique and technologically compelling properties, including strong confinement, in-plane anisotropy, a hyperbolic dispersion that leads to extremely large wavevectors, and the possibility for in-plane beam steering.[56, 136, 137]

As a first step towards exploring this novel set of behaviors, we are seeking to experimentally demonstrate anisotropic, electrically tunable plasmon resonances in few-layer black phosphorus for the first time. To elucidate how we can access this response, we first calculate the dielectric function of few-layer black phosphorus in the mid to far

infrared. To do so, we use an anisotropic Drude model to calculate the components of the optical conductivity. Further details on the effective mass and other parameters are contained in Reference [56].

$$\sigma_{jj}(\omega) = \frac{iD_j}{\pi(\omega + \frac{i\eta}{\hbar})}, \qquad D_j = \pi e^2 \sum_i \frac{n_i}{m_j^i} \qquad (6.1)$$

This optical conductivity can then be used to calculate the dielectric function, using the static dielectric constant $\epsilon_{rel}$ and black phosphorus thickness $\Delta$.

$$\epsilon_{jj}(\omega) = \epsilon_{rel} + i\frac{\sigma_{jj}(\omega)}{\Delta\epsilon_0\omega} \qquad (6.2)$$

These results are presented in Figure 6.1. From this calculation, it is clear that, at experimentally accessible doping levels, 5 nm black phosphorus has a negative real permittivity through much of the mid to far-infrared for the armchair axis. In contrast, its real permittivity remains positive through much of this spectral regime for the zigzag axis. As a result, we expect 5 nm black phosphorus to host anisotropic plasmons through the mid to far-infrared, and hyperbolic plasmons – where the armchair axis acts as a metal, but the zigzag axis does not – in the smaller, higher-frequency regime highlighted in Figure 6.1.

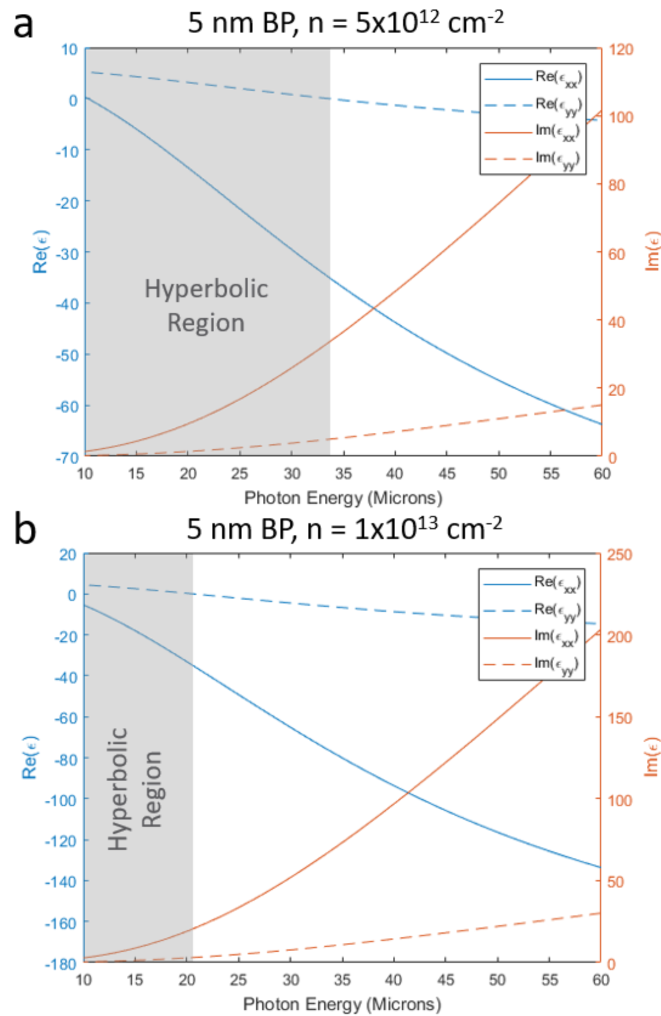


**Figure 6.1**: The calculated dielectric function for few-layer black phosphorus in the mid to far infrared, for both the armchair (xx) and zigzag (yy) axes. The hyperbolic regime, where the real part of the dielectric function is positive for one axis and negative for the other, is highlighted in grey. Both panels describe 5 nm black phosphorus, at **a)** $5 \times 10^{12}$ $cm^{-2}$ doping, and **b)** $1 \times 10^{13}$ $cm^{-2}$ doping.

As for surface plasmon modes in general, a grating or other nanostructure must be used to couple to these modes from free space. To generate this coupling, we pattern black phosphorus into nanoribbon resonators, similar to those previously used to observe plasmons in graphene.[11] We select ribbons with a range of widths of order 100 nm for straightforward fabrication, which prior theory results suggest should generate plasmon resonances at a wavelength of order 20 to 50 microns. Microspectroscopy is typically difficult in this regime, due to poor available sources and detectors. To enhance our signal

to noise ratio, we design a Salisbury screen style device with a backreflector to enhance the electric field intensity and thus light-matter interactions in the black phosphorus. Rather than the using the typical quarter wavelength resonance condition, we use higher order Fabry-Perot modes corresponding to optical path lengths of $L = m\lambda/4n$ (with $m =$ 5,7,9 within our spectral range of interest) to generate a higher spectral density of resonances to help interrogate the unknown black phosphorus plasmon resonance frequency. This device and FDTD simulation results that predict its resonant optical response are presented in Figure 6.2.

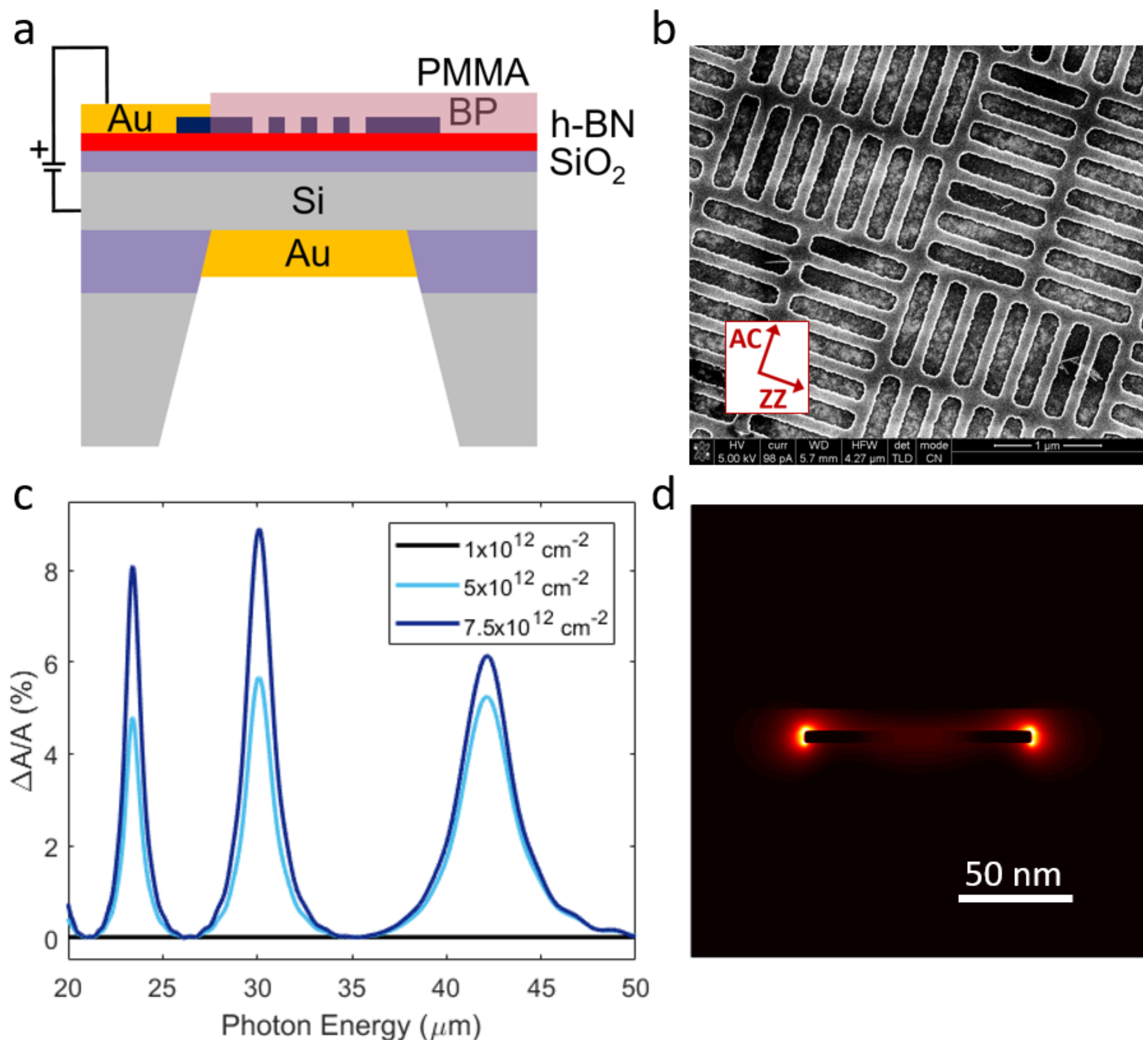


**Figure 6.2**: **a)** Schematic of gate-tunable black phosphorus plasmonic resonator device, including a silicon dielectric spacer and gold back reflector. **b)** Scanning electron microscope image of nanoribbons fabricated in few-layer black phosphorus, aligned to its

crystal axes. **c)** Simulated absorption modulation for 100 nm black phosphorus ribbons in the device geometry illustrated in **(a),** normalized to the $1x10^{12}$ $cm^{-2}$ doping case. The observed resonances are a convolution of spectrally narrow Fabry-Pérot modes due to the dielectric spacer and a single broad surface plasmon mode. **b)** Electric field intensity profile surrounding an individual nanoribbon at 30 microns for $7.5x10^{12}$ $cm^{-2}$ doping.

The silicon membrane device is first fabricated, as described in the Appendix, on silicon on insulator chips with a commercially grown, 50 nm top silicon oxide gate dielectric. A layer of hexagonal boron nitride is transferred on top of the silicon oxide, to improve the mobility of black phosphorus devices by screening interfacial trap states. A black phosphorus flake is then exfoliated onto PDMS and transferred to the membrane, after which standard fabrication techniques are used to complete the device, again as described in the Appendix. PMMA or h-BN encapsulation is used to protect the black phosphorus during the latter steps of fabrication and during measurements.

To experimentally characterize infrared absorption modulation in the mid to far infrared, an FTIR spectrometer coupled to an infrared microscope is used, with a helium-cooled, silicon bolometer detector. Initial results are presented in Figure 6.3. Clear, repeatable absorption modulation with electrostatic doping is observed for armchair axis polarization. This modulation may derive from multiple sources, including the black phosphorus plasmon, but also resonantly enhanced silicon free carrier absorption, or black phosphorus free carrier absorption. These results are encouraging, but more observations, ideally with a better signal to noise ratio, are necessary to prove the existence of a black phosphorus plasmon.

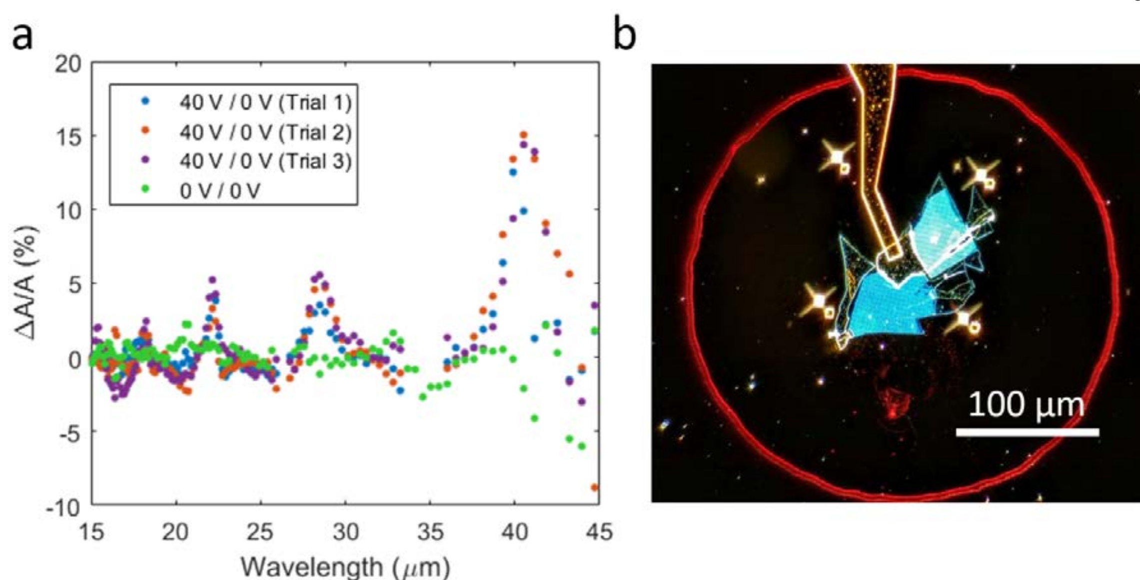


**Figure 6.3**: **a)** Armchair axis absorption modulation measured in 100 nm black phosphorus nanoribbons on a Salisbury screen device, as described in Figure 6.2. Three separate trials indicate nearly identical absorption modulation with doping, while the (green) baseline without doping shows zero modulation. **b)** A dark field optical microscope image of a completed nanoribbon Salisbury screen device. The large red circle is the rim of the silicon membrane, the yellow finger extending down from the top is a gold contact, and the bright blue regions are the nano-patterned portion of the black phosphorus flakes.

Thus far, these experiments have proved difficult for two reasons, which we propose a plan to resolve below. First and foremost, the signal to noise ratio achievable in the 40 to 50 micron range is low, despite any conceivable experimental accommodations. To mitigate this problem, we propose to fabricate ribbons with a smaller width in order to push the black phosphorus plasmon resonance to higher frequency. Process optimization will be necessary, but with a more carefully controlled reactive ion etching process, ribbon widths as small as 25 nm should be achievable. The plasmon resonance wavelength scales with $\sqrt{W}$, for ribbon width $W$, so we can likely shrink the (free space) resonance wavelength by a factor of two. The brightness of thermal FTIR sources improves dramatically at higher frequencies, and as do several other important factors. If successful, the resulting increase in experimental sensitivity may preclude the need for a Salisbury screen design, greatly simplifying device fabrication.

Second, the silicon bolometer microspectroscopy apparatus described above is, as of now, available only at the Advanced Light Source at Lawrence Berkeley National Lab. While using a synchrotron beam provides the benefit of a diffraction-limited spot size, it poses logistical challenges for rapid iteration of device design and measurement that slow experimental progress. For this reason, we are constructing a similar apparatus at Caltech, using a newer FTIR spectrometer, again coupled to an infrared microscope and helium-cooled silicon bolometer. An immediate, first experimental goal will be to demonstrate tunable, resonant absorption that differs between the armchair and zigzag crystal axes, indicating modulation of the black phosphorus plasmon.

### 6.1.2 Phase Modulation and Beam Steering in Black Phosphorus

The theory results we present in Chapter 5 suggest that few-layer black phosphorus is an outstanding material platform for phase modulation, beam steering, and active polarization control. We next seek to confirm this theory experimentally, to both prove out the predicted optoelectronic response of black phosphorus and make the case for the aforementioned technology applications.

Our theory work from Chapter 5 relies mostly on analytical calculations, which we expect to be highly robust, and a well-understand nanophotonic device design. However, the tunable complex index of refraction for few-layer black phosphorus is derived from theory, and represents a relatively unknown quantity that must be experimentally probed.[60] Our previous infrared studies of black phosphorus indicate that absorption in few-layer black phosphorus is strongly modulated by both band filling and the quantum-confined Stark effect, but do not quantify the index change. Further, existing theory predicts the electrically tunable refractive index of few-layer black phosphorus for only a single thickness, 5 nm. We plan to expand this theory to additional thicknesses, which we expect to host substantially different index tuning due to the varying band structure, Stark coefficient, and impact of band bending. Lastly, we propose to fabricate and measure a simple phase modulation structure.

The refractive index of a small flake of a two-dimensional materials is difficult to probe via traditional techniques like ellipsometry. Even with large exfoliated flakes and focusing probes, the spot size for a spectroscopic ellipsometer like the Woollam VASE is several times larger than the flake area. Three approaches might be used to solve this problem. First, it is possible to simply incorporate both the flake and background material into an "island-film" model while applying gate voltages, as described in Reference [138]. Similar modeling techniques have been used to characterize exfoliated graphene flakes, while other groups have developed higher resolution nano-ellipsometry.[139, 140] Second, the area surrounding the black phosphorus flake could be roughened to induce scattering, limiting the reflected signal to that of the flake. One way to achieve this roughening would be to use lithography to mask the flake while etching the surrounding material (with, for example, an HF dip to remove silicon oxide, followed by a short XeF2 etch to roughen the underlying silicon). Lastly, the flake could be surrounded by a deposited gold aperture, allowing transmission ellipsometry to probe only the flake and underlying substrate.

As these techniques are all relatively complex, we propose instead to simply measure absolute reflectance from gated black phosphorus devices, and then use a Kramers-Kronig constrained fitting methodology to fit the complex refractive index. This approach has been used successfully for gated, small-area flakes of $MoS_2$ and other materials.[132] To allow a nearly normal angle of incidence and absolute reference, we propose to use a supercontinuum laser source configured for small areas measurements in the Atwater lab with a pair of new InGaAs detectors to allow measurements out to 2.5 microns.

In coordination with this experimental investigation of the tunable refractive index of few-layer black phosphorus, we propose to expand corresponding theory to both match our findings and characterize multiple thicknesses of black phosphorus. One viable theoretical framework has been described in Reference [60], combining a self-consistent Schrödinger-Poisson calculation with the Kubo optical conductivity model outlined earlier in this thesis. It should be straightforward to apply this same methodology, plus any more accurate,

experimentally-informed bandstructure details to black phosphorus flakes of a range of thicknesses.

Lastly, if the experimentally observed refractive index tuning appears promising, we propose to experimentally demonstrate the modulation concepts described above. A first step would be to fabricate the resonant structures shown in Figures 5.2 and 5.3, and measure their amplitude and phase modulation. Reflectance amplitude modulation measurements are trivial with a suitable spectroscopy apparatus, and phase measurements can be performed via interferometry, as described in References [89] and [87]. To expand upon these initial device functions, measurements of phased array beam steering, electrically tunable polarization, or electrically tunable retarding should be performed.

### 6.1.3 Spin-Plasmons in Bismuth Antimony Telluride

As described in the Introduction, plasmon excitation of the surface carriers in 3D, electronic topological insulators is predicted to manifest in hybrid spin-charge collective modes, known as spin-plasmons.[21] Research progress in this area – of great interest to both the spintronics and nanophotonics communities – has been slow due to the difficulty of isolating the surface and bulk optical responses.[20] However, Dirac carriers and typical massive carriers should yield plasmons that exhibit fundamentally different dispersion relations with charge density, as demonstrated in prior work by on graphene plasmons by our group and others.[11] By clearly isolating the Dirac response in a topological insulator, we can create a platform to access more exotic spin-plasmon behavior.

To this end, we first propose to experimentally demonstrate Dirac surface plasmon modes in layered bismuth antimony telluride, by observing a Dirac dependence of the plasmon resonance frequency on carrier concentration – $\omega_p \propto n^{1/4}$ rather than $\omega_p \propto n^{1/2}$. In prior work described earlier in this thesis, we have shown by infrared microspectroscopy that the optical properties of BST can be modulated via electrostatic gating.[100] To help isolate the surface carrier response, we have fabricated top-gated, 5 nm BST devices from films grown epitaxially on sapphire by collaborators at Tsinghua University, with the Fermi level

positioned inside the bulk band gap.[16] We will fabricate similar devices with BST patterned by electron beam lithography and reactive ion etching into 100 nm ribbon resonators, and measure FTIR transmittance while varying the carrier density. We expect these modes to be visible in the mid to far infrared, near 30 microns for 100 nm resonators.

Once we have conclusively observed Dirac surface state plasmons, we plan to investigate the coupling between spin and charge degrees of freedom in these collective modes. We can observe evidence of spin-charge plasmon hybridization by optically exciting a pure spin wave in BST via a transient spin grating, then detecting any plasmons scattered to free space by a nearby resonator structure etched into the film. The hybridization of spin and charge – and hence the coupling efficiency of this measurement – is also predicted to be gate-tunable in thin topological insulator films. For films with identical charge density at the top and bottom surfaces, pure spin and charge modes are seen; as these carrier densities diverge, the two modes hybridize.[141] In this experiment, we could use a Ti:sapphire laser to illuminate the surface of a BST film with two noncollinear beams with orthogonal, linear polarizations to generate a transient spin grating.[21] The pitch of this grating is controlled by the phase difference between these beams, which we would use to match the plasmon wavelength to the resonator structure. We would then detect the light coupled to free space by this structure with an FTIR microscope operating in reflectance mode, as done in prior work by our team. These experiments would represent the first observation of spin-plasmons in a topological insulator, and present a fundamentally new type of collective mode for future investigations and possible incorporation into next-generation optoelectronic devices.

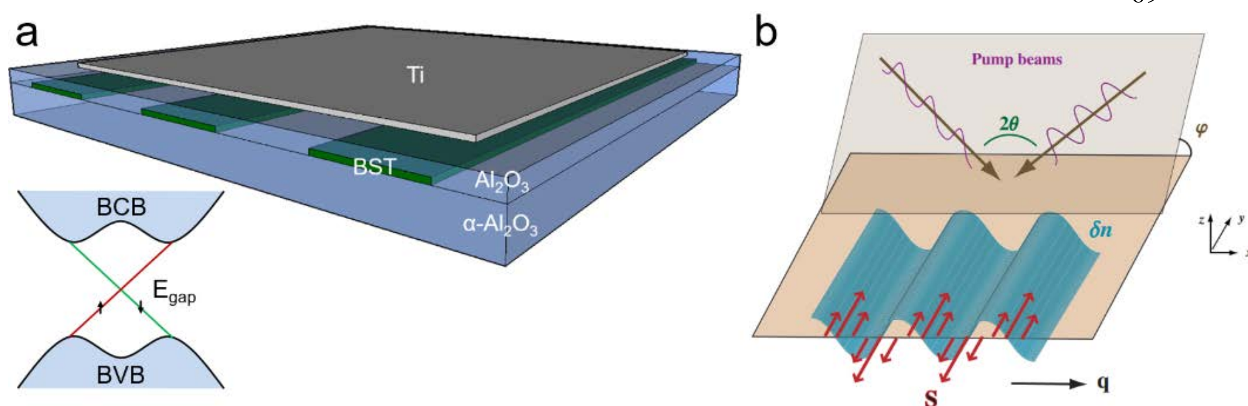


**Figure 6.4**: **a)** Structure for observation of gate-tunable Dirac plasmons in BST. The gate voltage is applied between the BST and a thin Ti top electrode on an ALD alumina gate. Incident light is linearly polarized with the electric field along the width of the BST ribbons. Inset: Schematic band structure of a 3D topological insulator. For BST, $E_{gap}$ = 0.3 eV. **b)** Schematic of experiment to observe spin-charge plasmon hybridization, from Reference 21. Two incident, noncollinear beams with orthogonal polarization strike the BST surface, generating a transverse pure spin wave that propagates as a spin-plasmon and scatters to free space from a ribbon grating.

### 6.2 Perspective

As we have demonstrated in this thesis, understanding the fundamental dynamics of light-matter interactions in new materials illuminates new physics, and may enable a host of new technology applications. For example, electrically-tunable light-matter interactions in van der Waals materials are a promising building block for next generation active photonic devices, including sources, detectors and modulators for telecommunications; beam-steering platforms for solid-state lidar and free space optical communications; and much more. In another recent, exciting effort, we have identified new nanophotonic structures incorporating both two-dimensional and bulk materials that may enable interstellar travel by ultra-light, laser-accelerated light sails.[142] The emerging materials explored here, and others, are likely candidates for enabling and improving the performance of many of these devices beyond that achievable with conventional materials.

However, an equally important goal for quantum materials, and all novel materials, is to consider what fundamentally new functionality might be generated by the new physics they

host. In few-layer black phosphorus, for example, we have seen that electrically-tunable birefringence and dichroism – a phenomenon we know of in no other materials – can enable dynamic polarization control in a fundamentally new way. A simple optical modulator loaded with this material can act as a tunable linear polarizer, a tunable retarder, and perhaps other device concepts we have yet to consider. In the future, devices that incorporate topological insulator materials may allow the control of spin; low loss, highly confined plasmon modes; or more exotic behavior.

The intersection of condensed matter physics and nanophotonics is a rich landscape for the discovery of new physical phenomena. As an ambitious vision for this field, we should seek not only to uncover new physics and identify promising mechanisms to achieve our technology goals. But, moreover, we should seek to continually reframe those goals in the context of what new physics we observe, and what may be expected in the future.

# Bibliography

1. Council, N. R., *Nanophotonics: Accessibility and Applicability*. The National Academies Press: Washington, DC, 2008; p 236.
2. Liu, Z.; Lee, H.; Xiong, Y., et al. *Science* **2007,** 315, (5819), 1686-1686.
3. Yu, N.; Capasso, F. *Nat Mater* **2014,** 13, 139.
4. Arbabi, A.; Horie, Y.; Bagheri, M., et al. *Nat Nanotechnol* **2015,** 10, 937.
5. Kildishev, A. V.; Boltasseva, A.; Shalaev, V. M. *Science* **2013,** 339, (6125).
6. Miller, D. A. B. *Proceedings of the IEEE* **2000,** 88, (6), 728-749.
7. Shen, Y.; Harris, N. C.; Skirlo, S., et al. *Nat Photonics* **2017,** 11, 441.
8. Novoselov, K. S.; Mishchenko, A.; Carvalho, A., et al. *Science* **2016,** 353, (6298).
9. Xia, F.; Wang, H.; Xiao, D., et al. *Nat Photonics* **2014,** 8, 899.
10. Xia, F.; Wang, H.; Jia, Y. *Nat Commun* **2014,** 5, 4458.
11. Brar, V. W.; Jang, M. S.; Sherrott, M., et al. *Nano Letters* **2013,** 13, (6), 2541-2547.
12. Li, Z. Q.; Henriksen, E. A.; Jiang, Z., et al. *Nature Physics* **2008,** 4, (7), 532-535.
13. Qi, X.-L.; Zhang, S.-C. *Reviews of Modern Physics* **2011,** 83, (4), 1057-1110.
14. Hasan, M. Z.; Kane, C. L. *Reviews of Modern Physics* **2010,** 82, (4), 3045-3067.
15. Kong, D.; Cui, Y. *Nat Chem* **2011,** 3, (11), 845-849.
16. Zhang, J.; Chang, C. Z.; Zhang, Z., et al. *Nat Commun* **2011,** 2, 574.
17. Chang, C.-Z.; Zhang, J.; Feng, X., et al. *Science* **2013,** 340, (6129), 167-170.
18. Valdés Aguilar, R.; Stier, A. V.; Liu, W., et al. *Physical Review Letters* **2012,** 108, (8), 087403.
19. McIver, J. W.; Hsieh, D.; Steinberg, H., et al. *Nat Nano* **2012,** 7, (2), 96-100.
20. Di Pietro, P.; Ortolani, M.; Limaj, O., et al. *Nat Nanotechnol* **2013,** 8, (8), 556-60.
21. Raghu, S.; Chung, S. B.; Qi, X. L., et al. *Phys Rev Lett* **2010,** 104, (11), 116401.
22. Lindner, N. H.; Farrell, A.; Lustig, E., et al. **2014.**
23. Whitney, W. S.; Sherrott, M. C.; Jariwala, D., et al. *Nano Letters* **2017,** 17, (1), 78-84.
24. Koppens, F. H. L.; Mueller, T.; Avouris, P., et al. *Nat Nanotechnol* **2014,** 9, (10), 780-793.
25. Sun, Z. P.; Martinez, A.; Wang, F. *Nat Photonics* **2016,** 10, (4), 227-238.
26. Wang, Q. H.; Kalantar-Zadeh, K.; Kis, A., et al. *Nat Nanotechnol* **2012,** 7, (11), 699-712.
27. Xia, F. N.; Wang, H.; Xiao, D., et al. *Nat Photonics* **2014,** 8, (12), 899-907.
28. Castellanos-Gomez, A. *The Journal of Physical Chemistry Letters* **2015,** 6, (21), 4280-4291.
29. Ling, X.; Wang, H.; Huang, S. X., et al. *P Natl Acad Sci USA* **2015,** 112, (15), 4523-4530.
30. Deng, Y.; Luo, Z.; Conrad, N. J., et al. *Acs Nano* **2014,** 8, (8), 8292-8299.
31. Xia, F. N.; Wang, H.; Jia, Y. C. *Nat Commun* **2014,** 5.
32. Liu, H.; Neal, A. T.; Zhu, Z., et al. *Acs Nano* **2014,** 8, (4), 4033-4041.
33. Du, Y.; Liu, H.; Deng, Y., et al. *Acs Nano* **2014,** 8, (10), 10035-10042.
34. Liu, H.; Du, Y.; Deng, Y., et al. *Chemical Society Reviews* **2015,** 44, (9), 2732-2743.

35. Buscema, M.; Groenendijk, D. J.; Blanter, S. I., et al. *Nano Letters* **2014,** 14, (6), 3347-3352.
36. Yuan, H. T.; Liu, X. G.; Afshinmanesh, F., et al. *Nat Nanotechnol* **2015,** 10, (8), 707-713.
37. Youngblood, N.; Chen, C.; Koester, S. J., et al. *Nat Photonics* **2015,** 9, (4), 247-252.
38. Engel, M.; Steiner, M.; Avouris, P. *Nano Letters* **2014,** 14, (11), 6414-6417.
39. Woomer, A. H.; Farnsworth, T. W.; Hu, J., et al. *Acs Nano* **2015,** 9, (9), 8869-8884.
40. Yang, J.; Xu, R. J.; Pei, J. J., et al. *Light-Sci Appl* **2015,** 4.
41. Zhang, S.; Yang, J.; Xu, R. J., et al. *Acs Nano* **2014,** 8, (9), 9590-9596.
42. Surrente, A.; Mitioglu, A. A.; Galkowski, K., et al. *Phys Rev B* **2016,** 94, (7).
43. Surrente, A.; Mitioglu, A. A.; Galkowski, K., et al. *Phys Rev B* **2016,** 93, (12).
44. Buscema, M.; Groenendijk, D. J.; Steele, G. A., et al. *Nat Commun* **2014,** 5.
45. Peng, C.; Jianyong, X.; Hua, Y., et al. *2D Materials* **2015,** 2, (3), 034009.
46. Jeon, P. J.; Lee, Y. T.; Lim, J. Y., et al. *Nano letters* **2016,** 16, (2), 1293-1298.
47. Wang, H.; Wang, X.; Xia, F., et al. *Nano Letters* **2014,** 14, (11), 6424-6429.
48. Likai Li, J. K., Chenhao Jin, Guojun Ye, Diana Y. Qiu, Felipe H. da Jornada, Zhiwen Shi, Long Chen, Zuocheng Zhang, Fangyuan Yang, Kenji Watanabe, Takashi Taniguchi, Wencai Ren, Steven G. Louie, Xianhui Chen, Yuanbo Zhang and Feng Wang. *arXiv:1601.03103* **2016**.
49. Wang, X. M.; Jones, A. M.; Seyler, K. L., et al. *Nat Nanotechnol* **2015,** 10, (6), 517-521.
50. Tran, V.; Soklaski, R.; Liang, Y. F., et al. *Phys Rev B* **2014,** 89, (23).
51. Kim, J.; Baik, S. S.; Ryu, S. H., et al. *Science* **2015,** 349, (6249), 723-6.
52. Brar, V. W.; Sherrott, M. C.; Jang, M. S., et al. *Nat Commun* **2015,** 6.
53. De Zoysa, M.; Asano, T.; Mochizuki, K., et al. *Nat Photon* **2012,** 6, (8), 535-539.
54. Bermel, P.; Ghebrebrhan, M.; Chan, W., et al. *Opt. Express* **2010,** 18, (S3), A314-A334.
55. Liu, M.; Yin, X.; Ulin-Avila, E., et al. *Nature* **2011,** 474, (7349), 64-67.
56. Low, T.; Roldán, R.; Wang, H., et al. *Physical Review Letters* **2014,** 113, (10), 106802.
57. Liu, Z.; Aydin, K. *Nano Letters* **2016,** 16, (6), 3457-3462.
58. Chaves, A.; Low, T.; Avouris, P., et al. *Phys Rev B* **2015,** 91, (15).
59. Low, T.; Rodin, A. S.; Carvalho, A., et al. *Phys Rev B* **2014,** 90, (7), 075434.
60. Lin, C.; Grassi, R.; Low, T., et al. *Nano Lett* **2016,** 16, (3), 1683-9.
61. Favron, A.; Gaufres, E.; Fossard, F., et al. *Nat Mater* **2015,** 14, (8), 826-+.
62. Tayari, V.; Hemsworth, N.; Fakih, I., et al. *Nat Commun* **2015,** 6.
63. Castellanos-Gomez, A.; Vicarelli, L.; Prada, E., et al. *2D Materials* **2014,** 1, (2).
64. Burstein, E. *Phys. Rev.* **1954,** 93, (3), 632-633.
65. Moss, T. S. *P Phys Soc Lond B* **1954,** 67, (418), 775-782.
66. Tian, H.; Guo, Q.; Xie, Y., et al. *Advanced Materials* **2016,** 28, (25), 4991-4997.
67. Miller, D. A. B.; Chemla, D. S.; Schmitt-Rink, S. *Phys Rev B* **1986,** 33, (10), 6976-6982.
68. Zhang, G.; Chaves, A.; Huang, S., et al. **2016.**
69. Guowei Zhang, A. C., Shenyang Huang, Chaoyu Song, Tony Low,; Yan, H. *arXiv:1607.08049* **2016**.

70. Sherrott, M. C.; Whitney, W. S.; Jariwala, D., et al. *Nano Letters* **2019,** 19, (1), 269-276.
71. Mak, K. F.; He, K.; Lee, C., et al. *Nat Mater* **2012,** 12, 207.
72. Fei, Z.; Rodin, A. S.; Andreev, G. O., et al. *Nature* **2012,** 487, (7405), 82-85.
73. Li, L.; Yu, Y.; Ye, G. J., et al. *Nat Nanotechnol* **2014,** 9, (5), 372-7.
74. Wang, T.; Hu, S.; Chamlagain, B., et al. *Advanced Materials* **2016,** 28, (33), 7162-7166.
75. Chen, C.; Youngblood, N.; Li, M. In *Study of black phosphorus anisotropy on silicon photonic waveguide*, 2015 Optoelectronics Global Conference (OGC), 29-31 Aug. 2015, 2015; pp 1-3.
76. Huang, M.; Wang, M.; Chen, C., et al. *Advanced Materials* **2016,** 28, (18), 3481-3485.
77. Chen, C.; Youngblood, N.; Peng, R., et al. *Nano Letters* **2017,** 17, (2), 985-991.
78. Liu, Y.; Qiu, Z.; Carvalho, A., et al. *Nano Letters* **2017,** 17, (3), 1970-1977.
79. Deng, B.; Tran, V.; Xie, Y., et al. *Nat Commun* **2017,** 8, 14474.
80. Peng, R.; Khaliji, K.; Youngblood, N., et al. *Nano Letters* **2017,** 17, (10), 6315-6320.
81. Zhang, G.; Huang, S.; Chaves, A., et al. *Nat Commun* **2017,** 8, 14071.
82. Wei, Q.; Peng, X. *Applied Physics Letters* **2014,** 104, (25), 251915.
83. Luo, Z.; Maassen, J.; Deng, Y., et al. *Nat Commun* **2015,** 6, 8572.
84. Liao, B.; Zhao, H.; Najafi, E., et al. *Nano Letters* **2017,** 17, (6), 3675-3680.
85. Lan, S.; Rodrigues, S.; Kang, L., et al. *ACS Photonics* **2016,** 3, (7), 1176-1181.
86. Qiao, J.; Kong, X.; Hu, Z.-X., et al. *Nat Commun* **2014,** 5, 4475.
87. Sherrott, M. C.; Hon, P. W. C.; Fountaine, K. T., et al. *Nano Letters* **2017,** 17, (5), 3027-3034.
88. Park, J.; Kang, J.-H.; Kim, S. J., et al. *Nano Letters* **2017,** 17, (1), 407-413.
89. Huang, Y.-W.; Lee, H. W. H.; Sokhoyan, R., et al. *Nano Letters* **2016,** 16, (9), 5319-5325.
90. Xu, Q.; Schmidt, B.; Pradhan, S., et al. *Nature* **2005,** 435, 325.
91. Kuo, Y.-H.; Lee, Y. K.; Ge, Y., et al. *Nature* **2005,** 437, 1334.
92. Inoue, T.; Zoysa, M. D.; Asano, T., et al. *Nat Mater* **2014,** 13, 928.
93. Coppens, Z. J.; Valentine, J. G. *Advanced Materials* **2017,** 29, (39), 1701275.
94. Moss, T. S. *Proceedings of the Physical Society. Section B* **1957,** 70, (2), 247.
95. Miller, D. A. B.; Chemla, D. S.; Damen, T. C., et al. *Physical Review Letters* **1984,** 53, (22), 2173-2176.
96. Ling, X.; Huang, S.; Hasdeo, E. H., et al. *Nano Letters* **2016,** 16, (4), 2260-2267.
97. Sim, S.; Lee, D.; Noh, M., et al. *Nat Commun* **2016,** 7, 13569.
98. Dolui, K.; Quek, S. Y. *Scientific Reports* **2015,** 5, 11699.
99. Chernikov, A.; van der Zande, A. M.; Hill, H. M., et al. *Physical Review Letters* **2015,** 115, (12), 126802.
100. Whitney, W. S.; Brar, V. W.; Ou, Y., et al. *Nano Letters* **2017,** 17, (1), 255-260.
101. Pesin, D.; MacDonald, A. H. *Nat Mater* **2012,** 11, (5), 409-416.
102. Jenkins, G. S.; Schmadel, D. C.; Sushkov, A. B., et al. *Phys Rev B* **2013,** 87, (15), 155126.
103. Post, K. W.; Chapler, B. C.; Liu, M. K., et al. *Phys Rev Lett* **2015,** 115, (11), 116804.

104. Wu, J.-S.; Basov, D. N.; Fogler, M. M. *Phys Rev B* **2015,** 92, (20), 205430.
105. Song, J. C. W.; Rudner, M. S. *Proceedings of the National Academy of Sciences* **2016,** 113, (17), 4658-4663.
106. Reijnders, A. A.; Tian, Y.; Sandilands, L. J., et al. *Phys Rev B* **2014,** 89, (7), 075138.
107. Jenkins, G. S.; Sushkov, A. B.; Schmadel, D. C., et al. *Phys Rev B* **2010,** 82, (12), 125120.
108. Grigorenko, A. N.; Polini, M.; Novoselov, K. S. *Nat Photon* **2012,** 6, (11), 749-758.
109. Boltasseva, A.; Atwater, H. A. *Science* **2011,** 331, (6015), 290-291.
110. Sun, Z.; Martinez, A.; Wang, F. *Nat Photon* **2016,** 10, (4), 227-238.
111. Brahlek, M.; Koirala, N.; Bansal, N., et al. *Solid State Communications* **2015,** 215–216, 54-62.
112. Bansal, N.; Cho, M. R.; Brahlek, M., et al. *Nano Lett* **2014,** 14, (3), 1343-8.
113. Yang, F.; Taskin, A. A.; Sasaki, S., et al. *Acs Nano* **2015,** 9, (4), 4050-4055.
114. Chen, J.; Qin, H. J.; Yang, F., et al. *Physical Review Letters* **2010,** 105, (17), 176602.
115. Zhang, W.; Yu, R.; Zhang, H.-J., et al. *New Journal of Physics* **2010,** 12, (6), 065013.
116. Li, Z.; Carbotte, J. P. *Phys Rev B* **2013,** 87, (15), 155416.
117. Rosenbaum, T. F.; Milligan, R. F.; Paalanen, M. A., et al. *Phys Rev B* **1983,** 27, (12), 7509-7523.
118. Moss, T. S. *Proc. Phys. Soc. London, Sect. B* **1954,** 67, (10), 775.
119. Mak, K. F.; Ju, L.; Wang, F., et al. *Solid State Communications* **2012,** 152, (15), 1341-1349.
120. Lin, C.; Grassi, R.; Low, T., et al. *Nano Lett.* **2016,** 16, (3), 1683-1689.
121. Lynch, D. *The Infrared Spectral Signature of Water Ice in the Vacuum Cryogenic AI&T Environment*; AEROSPACE CORP EL SEGUNDO CA: 2005.
122. Chen, Y. L.; Analytis, J. G.; Chu, J.-H., et al. *Science* **2009,** 325, (5937), 178-181.
123. Falkovsky, L. A. *Journal of Physics: Conference Series* **2008,** 129, 012004.
124. Kittel, C., *Introduction to Solid State Physics*. Wiley: 2004.
125. Schwierz, F. *Nat Nano* **2010,** 5, (7), 487-496.
126. Yeh, P., *Optical Waves in Layered Media*. Wiley: 2005.
127. Fatemi, V.; Hunt, B.; Steinberg, H., et al. *Physical Review Letters* **2014,** 113, (20), 206801.
128. Mak, K. F.; Shan, J. *Nat Photon* **2016,** 10, (4), 216-226.
129. Seibel, C.; Bentmann, H.; Braun, J., et al. *Physical Review Letters* **2015,** 114, (6), 066802.
130. Rönnlund, B.; Beckman, O.; Levy, H. *Journal of Physics and Chemistry of Solids* **1965,** 26, (8), 1281-1286.
131. Zheng, G.; Mühlenbernd, H.; Kenney, M., et al. *Nat Nanotechnol* **2015,** 10, 308.
132. Yu, Y.; Yu, Y.; Huang, L., et al. *Nano Letters* **2017,** 17, (6), 3613-3618.
133. Ozbay, E. *Science* **2006,** 311, (5758), 189.
134. Schuller, J. A.; Barnard, E. S.; Cai, W., et al. *Nat Mater* **2010,** 9, 193.
135. Huber, M. A.; Mooshammer, F.; Plankl, M., et al. *Nat Nanotechnol* **2016,** 12, 207.
136. Nemilentsau, A.; Low, T.; Hanson, G. *Physical Review Letters* **2016,** 116, (6), 066804.

137. Correas-Serrano, D.; Gomez-Diaz, J. S.; Melcon, A. A., et al. *Journal of Optics* **2016,** 18, (10), 104006.
138. Fujiwara, H., *Spectroscopic Ellipsometry: Principles and Applications*. Wiley: 2007.
139. Kravets, V. G.; Grigorenko, A. N.; Nair, R. R., et al. *Phys Rev B* **2010,** 81, (15), 155413.
140. Wurstbauer, U.; Röling, C.; Wurstbauer, U., et al. *Applied Physics Letters* **2010,** 97, (23), 231901.
141. Stauber, T.; Gómez-Santos, G.; Brey, L. *Phys. Rev. B* **2013,** 88, (20), 205427.
142. Kildishev, A. V.; Boltasseva, A.; Shalaev, V. M. *Science* **2013,** 339, (6125), 1232009.
143. Lin, W.-H.; Brar, V. W.; Jariwala, D., et al. *Chemistry of Materials* **2017,** 29, (11), 4700-4707.
144. Chen, X.; Wu, Y.; Wu, Z., et al. *Nat Commun* **2015,** 6, 7315.
145. Wood, J. D.; Wells, S. A.; Jariwala, D., et al. *Nano Letters* **2014,** 14, (12), 6964-6970.
146. Mao, N.; Tang, J.; Xie, L., et al. *Journal of the American Chemical Society* **2016,** 138, (1), 300-305.

# Appendix A: Nanofabrication Methods

### A.1: Exfoliation of Black Phosphorus and Boron Nitride Crystals

Black phosphorus and hexagonal boron nitride flakes were exfoliated in a glove box from crystals grown by HQ Graphene. A variety of tapes were used to maximize the size of exfoliated flakes. When necessary for making van der Waals heterostructures, black phosphorus or hexagonal boron nitride flakes were directly exfoliated onto PDMS substrates, then transferred with use of a microscope, translation stages and a heater to the target substrate. For direct exfoliation to thermal oxide on silicon, substrates were pre-treated with Nano-Strip solution immediately beforehand to encourage hydrophilicity and improve adhesion.

### A.2: Wet Transfer of Hexagonal Boron Nitride

Hexagonal boron nitride films are grown on copper foils, as reported elsewhere.[143] PMMA is spun onto the top surface of the foil, and the boron nitride is removed from its bottom side via plasma ashing. The foil is then floated, with its top surface up, on a solution of copper etchant (ferric chloride) until all of the copper is dissolved. The PMMA-supported boron nitride films are then scooped with a spoon onto clean water in four stages, and finally scooped up with the target substrate. The chips are then dried on a hot plate at 45 C overnight, after which the PMMA is removed with acetone and IPA.

### A.3: Identification of Black Phosphorus Flake Thickness

Black phosphorus flake thicknesses are first qualitatively estimated by comparing their color and contrast on a given substrate to that of previously characterized flakes. On most substrates, including the 285 nm thermal oxide on silicon wafers used for many of the experiments described here, few-layer black phosphorus appears blue – a darker shade for one to five nanometers thick, a lighter shade for five to ten nanometers, and a very light blue that approaches white for ten to fifteen nanometers. For quantitative characterization, atomic

force microscopy or infrared spectroscopy are used. Atomic force microscopy typically overestimates the thickness of black phosphorus flakes, due to the presence of phosphorus oxide at both interfaces for all but perfect encapsulation. Infrared spectroscopy requires a catalog of intersubband optical transition energies for different thicknesses, as is presented in Reference [81].

**A.4: Encapsulation of Black Phosphorus**

Black phosphorus degrades rapidly (significant degradation after 1 hour) in air, so must be encapsulated for high performance devices. Several encapsulation mechanisms can be used, including capping with hexagonal boron nitride, deposition of $Al_2O_3$ via atomic layer deposition, and spin-coating with PMMA. Capping with h-BN is highly effective, but requires small area devices.[144] Deposition of $Al_2O_3$ is also highly effective, but must be done using a special recipe and may induce light damage to the top-most layer of black phosphorus.[145] Spin-coating with PMMA is only moderately effective, but simplifies sample processing.[62] An encapsulation layer of boron nitride underneath the black phosphorus additionally screens interfacial trap states, preventing unintended doping and increasing mobility in the black phosphorus flake.

**A.5: Identification of Black Phosphorus Crystal Axes**

The x (armchair) and y (zig-zag) crystal lattice directions are determined by polarization-dependent visible reflectance measurements. At each angle of polarization an image is recorded, and pixel RGB values are sampled from both the BP flake and nearby substrate. The ratio of green channel values from flake to substrate is averaged over three sample positions, and plotted as a function of polarization angle. Maxima and minima in green reflectance determine the armchair and zig-zag directions, respectively.[146] Alternatively, cross-polarization microscopy was used to identify crystal axes. Light passes through a linear polarizer, reflects from the sample, and passes through a second, orthogonal linear polarizer en-route to the eyepiece. The sample is placed on a rotating stage, and when reflected intensity is minimized, the crystal axes are

aligned to the polarization axes of the microscope. The two axes can then be determined as armchair or zig-zag based on Raman or infrared spectroscopy.

**A.6: Lithography and Metallization of Device Contacts**

The fabrication of metal contacts to black phosphorus and bismuth antimony telluride is achieved by a combination of electron beam lithography, metal deposition, and lift-off. For large area bismuth antimony telluride films, this is a single step process. Typically, 950 PMMA A8 is spun at 3000 rpm for 60 seconds, baked at 180 C for two minutes, and then written (EBPG 5000+) with a 50 nA beam current and dose of approximately 1600 μC/cm$^2$, plus an appropriate proximity error correction. This pattern is developed in a 3:1 mixture of IPA:MIBK for approximately 30 to 60 seconds, checking the development process under a microscope as necessary. A thin adhesion layer of 5 nm Ti or Cr is deposited, followed by 250 nm or more of gold. To prevent shorts in gated devices from damage during wire bonding, as much as 500 nm of gold can be used. The non-patterned metal is then lifted off in Remover PG or acetone for four hours, followed by rinsing in IPA. If Remover PG is used, multiple cycles of Remover PG, then IPA, etc., are used to prevent any remnant film. For the fabrication of contacts to small area black phosphorus flakes, a multi-step alignment process is used.

For this process, an array of alignment marks is first deposited on the target substrate, typically 20 μm x 20 μm squares spaced 1.5 mm apart in a 2D grid, using the process outlined above. Next, flakes are exfoliated to this substrate and identified in a microscope. Then, a target flake is located in the EBPG alignment microcope, and its position noted. A small array of reference markers is then written (EBPG 5000+), centered on the target flake, using an aligned write aligned to the larger array of alignment marks. This smaller array of reference marks typically consists of four 5 μm x 5 μm marks spaced 100 μm apart in a 2D grid. Metal is deposited and lifted off, and a microscope image is taken centered on the target flake. This image is then imported to a CAD file containing an identical set of four marks and aligned to those marks, after which contacts can be drawn in CAD overlaid on top of the

image of the flake, then fabricated. This technique allows accurate fabrication of metal contacts to small flakes, to within 0.5 μm lateral position.

### A.7: Lithography and Etching of Black Phosphorus Nanoribbons

Black phosphorus nanoribbons were fabricated by a combination of electron beam lithography and reactive ion etching. A 1:1 mixture of ZEP 520A resist and anisole is spun at 2000 rpm for 60 seconds, then baked at 180 C for three minutes. A ribbon pattern, aligned to the crystal axes of the black phosphorus, is written in an EBPG 5000+ with a 300 pA electron beam and 200 $\mu C/cm^2$ dose, plus an appropriate proximity error correction. After exposure, the pattern is developed for 60 seconds in ZED N50 developer at room temperature, followed by 30 seconds in IPA. The samples are then post-baked at 110 C for 5 minutes, in air.

Next, the ribbon pattern is etched in a Plasmatherm reactive ion etching system. The etch recipe is 15 mTorr pressure, 20 sccm Ar and 10 sccm $SF_6$, 45 W power, and approximately 30 seconds etch time. It is critical to pre-condition the system chamber by running this same etch, with a time of at least 1 minute, immediately before loading the sample. Otherwise, the system may strike plasma much earlier, resulting in highly variable etch results. After etching, the resulting nanoribbons should be characterized by scanning electron microscopy. This etch is fast, and better results may be had by changing the chemistry or power to slow it down to allow optimization.

### A.8: Fabrication of Silicon Membranes

Silicon quarter wave resonators are fabricated using commercially acquired insulator on silicon on insulator wafers, which are first diced into 1 cm x 1 cm pieces. The silicon on insulator device layer is then protected by spinning a thick layer of PMMA resist. One layer of 950 PMMA A11 is spun at 3000 rpm for 60 seconds, baked for two minutes at 180 C, and removed from heat, before a second layer is spun on top of the first with the same recipe. The chip is then flipped, and a single layer of 950 PMMA A11 is spun on the handle side,

with the same recipe. A single 250 μm x 250 μm square is written in the center of the handle side resist, using the EBPG 5000+ (50 nA beam, 1800 $\mu C/cm^2$ dose, appropriate proximity error correction), and then developed in a 3:1 mixture of IPA:MIBK for 30 to 60 seconds, as necessary. The samples are then dipped in buffered hydrofluoric acid, followed by three stages of water, to strip the silicon oxide from the surface of the handle layer (the etch rate is approximately 80 nm per minute).

Next, a dedicated $XeF_2$ dry etch system is used to etch through the handle layer to the buried oxide. The samples are placed with the (now protected) device side face down on Kapton tape on a glass slide, and etched with an etch pressure of 2000 mT, pumping pressure of 80 mT, purge duration of 10 sec, and purge quantity of 5. For a handle thickness of approximately 350 microns, a first set of 50 etch pulses at 40 seconds etch, followed by examination under an optical microscope. Next, sets of 10 etch pulses at 40 seconds each are used, with examination between each set, until a sufficient etch hole is observed so as to clearly expose a large enough area of the buried oxide layer. The etch rate of this tool is variable, so the timing must be re-characterized frequently.

Next, all PMMA is removed with PG Remover and IPA, and a fresh bi-layer of PMMA is spun on top of the device layer. Then, the buried oxide is removed with a second hydrofluoric acid dip, followed by three stages of water. To allow the acid to wet into the hole etched by the $XeF_2$ dry etch, the samples must first be treated with a solution Triton X-100 surfactant heavily diluted with water. A Filmetrics tool can be used to confirm that the oxide has been removed entirely. A color change should also be noticeable in a microscope.

The chips are then flipped, and a 5 nm adhesion layer and 200 nm gold layer are deposited on the underside of the now-exposed silicon membrane. The PMMA is again removed with PG Remover and IPA. Another water rinse may be used to ensure that no hydrofluoric acid residue remains.

# Appendix B: Calculation Methods

### B.1: Black Phosphorus Optical Conductivity Calculation (Matlab)

```
%%% Optical conductivity calculation for few-layer black phosphorus
%%% William S. Whitney (wwhitney@caltech.edu)
%%% Based on calculation by Tony Low, et al., in doi:10.1103/PhysRevB.90.075434
%%% Please read that paper for details on the physics, including
%%% approximations and constants, and normalization of the output

% Physical constants
h = 4.135668e-15; % planck's constant in ev
hb = h/(2*pi); % reduced planck's constant in ev
hbj = 1.054571e-34; % reduced planck's constant in joules
c = 2.9979e8; % speed of light
e = 1.6021766e-19; % elementary charge, in coulombs
m0 = 9.10938e-31; % electron mass, in kg
eps0 = 8.854187e-12; % permittivity of free space

% Parameters to change.  User must set these, and data / plotting file names at end
tz = 5e-9; % flake thickness
axis = 'xx'; % crystal / polarization axis ('xx' or 'yy')
egap = 0.62; % band gap
T = 80; % temperature, in k
aryhbwj = linspace(0.4*e,1*e,100); % frequency band for calculation, in ev
kpartitions = 1000; % points to sample in k space (numerical instabilities below 1000 or so)
intsubbands = 10; % number of subbands to sum over (too many = slow, too few = large inaccuracies)
pp = parpool(32) % set up parallel computing resource (machine dependent, read appropriate manpages)

% Setup
a = 4.47e-10/2; % using low / lin convention
b = 3.34e-10/2; % using low / lin convention
Ev = -0.3*e; % bulk band energies, set Ec to 0
Ec = 0*e;
etac = (hbj^2)/(0.4*m0);
etav = (hbj^2)/(0.4*m0);
nuc = (hbj^2)/(1.4*m0);
nuv = (hbj^2)/(2.0*m0);
gamma = e*4*a/pi;
beta = e*2*(a^2)/(pi^2);
etad = 5e-3*e;
mvz = 0.46*m0; % valence eff mass, from Lin, NL 2016
mcz = 0.25*m0; % cond eff mass, from Lin, NL 2016
dgap = egap - ((Ec + hbj*hbj*pi*pi/(2*mcz*tz*tz))-(Ev - hbj*hbj*pi*pi/(2*mvz*tz*tz)))/e;
dsc = 1*e*dgap/2;
dsv = 1*e*dgap/2;
deltaEv1 = (hbj^2)*(pi^2)/(2*mvz*(tz^2)) + dsv;
deltaEc1 = (hbj^2)*(pi^2)/(2*mcz*(tz^2)) + dsc;
Ec1 = Ec + deltaEc1;
```

```
Ev1 = Ev - deltaEv1;
Ef = (Ec1 + Ev1)/2;
kbsi = 1.38064852e-23;
kT = kbsi*T;
aryw = aryhbwj./hbj;
arykx = linspace(-pi/a,pi/a,kpartitions);
aryky = linspace(-pi/b,pi/b,kpartitions);
arys = [1 -1];
arysp = [-1 1];
aryj = 1:intsubbands;
arysigxx = zeros(1,length(aryw));

% Start calculating
% Loop over frequencies
for idxw = 1:length(aryw)
  fltSum = 0;
  hbwj = aryhbwj(idxw);
  fltPctDone = 100*idxw/length(aryw);
  disp(sprintf('%0.1f%% Complete\n',fltPctDone));
  % Loop over s quantum number
  for idxs = 1:length(arys)
    % Loop over j quantum number
    for idxj = 1:length(aryj)
      s = arys(idxs);
      sp = arysp(idxs);
      j = aryj(idxj);
      deltaEvj = (j^2)*(hbj^2)*(pi^2)/(2*mvz*(tz^2)) + dsv;
      deltaEcj = (j^2)*(hbj^2)*(pi^2)/(2*mcz*(tz^2)) + dsc;
      Ecj = Ec + deltaEcj;
      Evj = Ev - deltaEvj;
      delj = Ecj - Evj;
      aryIntValskx = zeros(1,length(arykx));
      % Loop over kx
      parfor idxkx = 1:length(arykx) % this loop is parallelized, make regular for to debug
        aryIntValsky = zeros(1,length(aryky));
        kx = arykx(idxkx);
        % Loop over ky
        for idxky = 1:length(aryky)
          ky = aryky(idxky);
          Hj = [Ecj + etac*kx^2 + nuc*ky^2, gamma*kx + beta*ky^2;
            gamma*kx + beta*ky^2, Evj - etav*kx^2 - nuv*ky^2];
          if axis == 'xx'
            v = (1/hbj)*[2*etac.*kx gamma; gamma -2*etav.*kx];
          elseif axis == 'yy'
            v = (1/hbj)*[2*nuc.*ky 2*beta*ky; 2*beta*ky -2*nuv.*ky];
          else
            error('Bad axis specification!');
          end
          if (s == 1)
            Esjk = (1/2)*((Ecj + Evj) + (etac-etav)*kx^2 + (nuc-nuv)*ky^2) ...
              + (1/2)*((delj^2 + delj*(2*(etac+etav)*kx^2 + 2*(nuc+nuv)*ky^2)) ...
              + ((etac+etav)*kx^2 + (nuc+nuv)*ky^2)^2 + 4*(gamma*kx + beta*ky^2)^2)^(1/2);
            Phisjk = [ 1; (Esjk-Hj(1,1))/Hj(1,2)];
```

```
          Phisjk = Phisjk/norm(Phisjk);
        else
          Esjk = (1/2)*((Ecj + Evj) + (etac-etav)*kx^2 + (nuc-nuv)*ky^2) ...
            - (1/2)*((delj^2 + delj*(2*(etac+etav)*kx^2 + 2*(nuc+nuv)*ky^2)) ...
            + ((etac+etav)*kx^2 + (nuc+nuv)*ky^2)^2 + 4*(gamma*kx + beta*ky^2)^2)^(1/2);
          Phisjk = [ 1; (Esjk-Hj(1,1))/Hj(1,2)];
          Phisjk = Phisjk/norm(Phisjk);
        end
        if (sp == 1)
          Espjk = (1/2)*((Ecj + Evj) + (etac-etav)*kx^2 + (nuc-nuv)*ky^2) ...
            + (1/2)*((delj^2 + delj*(2*(etac+etav)*kx^2 + 2*(nuc+nuv)*ky^2)) ...
            + ((etac+etav)*kx^2 + (nuc+nuv)*ky^2)^2 + 4*(gamma*kx + beta*ky^2)^2)^(1/2);
          Phispjk = [ 1; (Espjk-Hj(1,1))/Hj(1,2)];
          Phispjk = Phispjk/norm(Phispjk);
        else
          Espjk = (1/2)*((Ecj + Evj) + (etac-etav)*kx^2 + (nuc-nuv)*ky^2) ...
            - (1/2)*((delj^2 + delj*(2*(etac+etav)*kx^2 + 2*(nuc+nuv)*ky^2)) ...
            + ((etac+etav)*kx^2 + (nuc+nuv)*ky^2)^2 + 4*(gamma*kx + beta*ky^2)^2)^(1/2);
          Phispjk = [ 1; (Espjk-Hj(1,1))/Hj(1,2)];
          Phispjk = Phispjk/norm(Phispjk);
        end
        fEsjk = 1/(exp((Esjk-Ef)/kT)+1);
        fEspjkp = 1/(exp((Espjk-Ef)/kT)+1);
        aryIntValsky(idxky) = ((fEsjk - fEspjkp)/(Esjk - Espjk)) ...
          *(transpose(Phisjk)*v*Phispjk)*(transpose(Phispjk)*v*Phisjk)/(Esjk-Espjk+hbwj+etad*1i);
      end
      aryIntValskx(idxkx) = trapz(aryky,aryIntValsky);
    end
    fltIntVal = -1i*2*hbj*e*e*trapz(arykx,aryIntValskx)/(4*pi*pi);
    fltSum = fltSum + fltIntVal;
  end
 end
 arysigxx(idxw) = fltSum/(e*e/(4*hbj));
end

% Generate plots and save data.  User must modify file names below
figure;
plot(aryhbwj/e,real(arysigxx));
xlabel('Photon Energy (eV)');
ylabel('Re(\sigma_{xx}/\sigma_{0})');
title(sprintf('Thickness: %0.1e nm',tz))
savefig('ReSigXXvsPhotonEnergy5nmIntEfExt'); % Choose appropriate file name
saveas(gcf,'ReSigXXvsPhotonEnergy5nmIntEfExt.jpg'); % Choose appropriate file name
figure;
plot(aryhbwj/e,imag(arysigxx));
xlabel('Photon Energy (eV)');
ylabel('Im(\sigma_{xx}/\sigma_{0})');
title(sprintf('Thickness: %0.1e nm',tz))
savefig('ImSigXXvsPhotonEnergy5nmIntEfExt'); % Choose appropriate file name
saveas(gcf,'ImSigXXvsPhotonEnergy5nmIntEfExt.jpg'); % Choose appropriate file name
save('dataxx5nmIntEf.mat','arysigxx','aryhbwj'); % Choose appropriate file name
```

## B.2: Black Phosphorus Microcavity Transfer Matrix Calculation (Lumerical)

```
### Transfer matrix calculation of multilayer stack reflectance amplitude and phase shift
### William S. Whitney (wwhitney@caltech.edu)
### Note: must use this .lsf file with a Lumerical .fsp file that includes all material data

### parameters to set
f = linspace(c/2390e-9, c/2405e-9,500); # frequency vector
pairs_top = 10; # number of top bragg reflector pairs
pairs_bottom = 40; # number of bottom bragg reflector pairs
operating_frequency = 2401; # cavity resonance frequency, in nm

### build stack
d = [0];
nf = length(f);
n1 = matrix(1,nf);
n1(1,1:nf) = 1; # air
# build top mirrors
for (i=1:pairs_top) {
d = [d; (operating_frequency/1550)*206e-9; (operating_frequency/1550)*268e-9];
n1add = matrix(1,nf);
n1add(1,1:nf) = 1.87;
n1 = [n1; n1add];
n1add = matrix(1,nf);
n1add(1,1:nf) = 1.45;
n1 = [n1; n1add];
}
# build active layer
d = [d; 5e-9]; # bp
n1add = matrix(1,nf);
n1add(1,1:nf) = getfdtdindex("BP 1e10 xx",f,min(f),max(f));
n1 = [n1; n1add];
active_size = size(n1);
d = [d; 10e-9]; # gate layer
n1add = matrix(1,nf);
n1add(1,1:nf) = 1.73;
n1 = [n1; n1add];
d = [d; (operating_frequency/1550)*190e-9]; # buffer layer
n1add = matrix(1,nf);
n1add(1,1:nf) = 1.87;
n1 = [n1; n1add];
# build bottom mirrors
for (i=1:pairs_bottom) {
d = [d; (operating_frequency/1550)*111.2e-9; (operating_frequency/1550)*127.6e-9];
n1add = matrix(1,nf);
n1add(1,1:nf) = 3.5;
n1 = [n1; n1add];
n1add = matrix(1,nf);
n1add(1,1:nf) = 3.05;
n1 = [n1; n1add];
}
# build substrate
```

```
d = [d; 500e-6]; # gaas
n1add = matrix(1,nf);
n1add(1,1:nf) = 3.55;
n1 = [n1; n1add];

# build tuned structure
n2 = n1;
n2(active_size(1),1:length(f)) = getfdtdindex("BP 1e12 xx",f,min(f),max(f));
n3 = n1;
n3(active_size(1),1:length(f)) = getfdtdindex("BP 5e12 xx",f,min(f),max(f));
n4 = n1;
n4(active_size(1),1:length(f)) = getfdtdindex("BP 1e13 xx",f,min(f),max(f));
n5 = n1;
n5(active_size(1),1:length(f)) = getfdtdindex("BP 1.5e13 xx",f,min(f),max(f));
n6 = n1;
n6(active_size(1),1:length(f)) = getfdtdindex("BP 1e10 yy",f,min(f),max(f));

# get RT using dispersive data (n1)
RT1 = stackrt(n1,d,f);
RT2 = stackrt(n2,d,f);
RT3 = stackrt(n3,d,f);
RT4 = stackrt(n4,d,f);
RT5 = stackrt(n5,d,f);
RT6 = stackrt(n6,d,f);

# generate plots
plot(RT1.lambda*1e6,RT1.Rp,RT2.Rp,RT3.Rp,RT4.Rp,RT5.Rp,RT6.Rp,"Wavelength
(um)","Power","Theta=0");
legend("R:xx,1e10","R:xx,1e12","R:xx,5e12","R:xx,1e13","R:xx,1.5e13","R:yy,1e10");
plot(RT1.lambda*1e6,(180/pi)*angle(RT1.rp),(180/pi)*angle(RT2.rp),(180/pi)*angle(RT3.rp),(180/pi)*an
gle(RT4.rp),(180/pi)*angle(RT5.rp),(180/pi)*angle(RT6.rp),(180/pi)*(angle(RT5.rp)-
angle(RT1.rp)),"Wavelength (um)","Reflection Phase","Theta=0");
legend("Phase:xx,1e10","Phase:xx,1e12","Phase:xx,5e12","Phase:xx,1e13","Phase:xx,1.5e13","Phase:yy,1
e10","Reflectance Modulation");
```